Persistence of bubble outlets in soft, methane-generating sediments

Citation: Scandella, Benjamin P.; Delwiche, Kyle; Hemond, Harold F. and Juanes, Ruben. "Persistence of Bubble Outlets in Soft, Methane-Generating Sediments." Journal of Geophysical Research: Biogeosciences 122 (June 2017): 1-26. © 2017 American Geophysical Union

As Published: http://dx.doi.org/10.1002/2016jg003717

Publisher: American Geophysical Union (AGU)

Persistent URL: http://hdl.handle.net/1721.1/110544

Version: Final published version: final published article, as it appeared in a journal, conference proceedings, or other formally published context

AGU PUBLICATIONS

JGR

Journal of Geophysical Research: Biogeosciences

RESEARCH ARTICLE
10.1002/2016JG003717

Key Points:
- Our novel incubation experiment allows direct imaging of bubble releases with centimeter-scale resolution
- Bubble outlets are reused both within ebullition events and over the scale of days to months
- Hydrostatic pressure plays a determinant role in enhancing and inhibiting ebullition

Supporting Information:
- Supporting Information S1

Correspondence to:
R. Juanes,
juanes@mit.edu

Citation:
Scandella, B. P., K. Delwiche, H. F. Hemond, and R. Juanes (2017), Persistence of bubble outlets in soft, methane-generating sediments, *J. Geophys. Res. Biogeosci.*, *122*, doi:10.1002/2016JG003717.

Received 15 NOV 2016
Accepted 16 APR 2017
Accepted article online 21 APR 2017

Persistence of bubble outlets in soft, methane-generating sediments

Benjamin P. Scandella[1], Kyle Delwiche[1], Harold F. Hemond[1], and Ruben Juanes[1,2]

[1]Department of Civil and Environmental Engineering, Massachusetts Institute of Technology, Cambridge, Massachusetts, USA, [2]Department of Earth, Atmospheric and Planetary Sciences, Massachusetts Institute of Technology, Cambridge, Massachusetts, USA

Abstract Sediments submerged beneath many inland waterways and shallow oceans emit methane, a potent greenhouse gas, but the magnitude of the methane flux to the atmosphere remains poorly constrained. In many settings, the majority of methane is released through bubbling, and the spatiotemporal heterogeneity of this ebullition both presents challenges for measurement and impacts bubble dissolution and atmospheric emissions. Here we present laboratory-scale experiments of methane ebullition in a controlled incubation of reconstituted sediments from a eutrophic lake. Image analysis of a 0.14 m^2 sediment surface area allowed identification of individual bubble outlets and resolved their location to ~1 cm. While ebullition events were typically concentrated in bursts lasting ~2 min, some major outlets showed persistent activity over the scale of days and even months. This persistence was surprising given the previously observed ephemerality of spatial structure at the field scale. This persistence suggests that, at the centimeter scale, conduits are reopened as a result of a drop in tensile strength due to deformation of sediments by the rising bubbles. The mechanistic insight from this work sheds light on the spatiotemporal distribution of methane venting from organic-rich sediments and has important implications for bubble survival in the water column and associated biogeochemical pathways of methane.

1. Introduction

Natural sources of methane to the atmosphere include sediments submerged in wetlands, lakes, man-made reservoirs, rivers, and oceans, but the magnitude of these emissions remains poorly constrained [*Kirschke et al.*, 2013]. Methane may be released either in its dissolved phase or as gas bubbles, which transport methane rapidly through the overlying water column and reduce the amount exposed to oxidation before reaching the atmosphere. In many settings, ebullitive fluxes deliver the majority of the atmospheric release [*Martens and val Klump*, 1980; *Kipphut and Martens*, 1982; *Crill et al.*, 1988; *Mattson and Likens*, 1990; *Keller and Stallard*, 1994; *Nakamura et al.*, 1999; *Bastviken et al.*, 2004; *Walter et al.*, 2006; *DelSontro et al.*, 2010; *Bastviken et al.*, 2011; *Maeck et al.*, 2013a], but estimating large-scale flux magnitudes is challenging because ebullition is particularly episodic and spatially heterogeneous [*Greinert*, 2008; *Ostrovsky et al.*, 2008; *Greinert et al.*, 2010; *Wik et al.*, 2011; *Varadharajan and Hemond*, 2012; *Maeck et al.*, 2013b; *Walter Anthony and Anthony*, 2013; *Bayrakci et al.*, 2014; *DelSontro et al.*, 2015; *Scandella et al.*, 2016].

The magnitude of the flux of methane to the atmosphere depends on the strength of the methane source but is also mediated by the dissolution of bubbles during their rise through the water column. During a bubble's rise to the surface, some portion of its methane dissolves into the surrounding water [*Rehder et al.*, 2002; *McGinnis et al.*, 2006; *Gong et al.*, 2009], and the dissolved methane may be either oxidized to carbon dioxide [*Rudd et al.*, 1974; *Nakamura et al.*, 1999], a greenhouse gas with lower global warming potential [*Forster et al.*, 2007], or transported to the surface by turbulent mixing. The amount of methane lost to dissolution depends on the initial size and release depth [*McGinnis et al.*, 2006], as well as the spatial and temporal concentration of gas release, because bubble plumes create upwelling currents and locally saturate the water with methane [*Leitch and Baines*, 1989; *Leifer et al.*, 2006; *Gong et al.*, 2009; *Wang et al.*, 2016]. Bubble dissolution may also depend on the mode of release because smaller bubbles dissolve faster [*McGinnis et al.*, 2006], and the bubble size distribution (BSD) may depend on the rate of gas release [*Greinert and Nutzel*, 2004; *Vallebuona et al.*, 2005].

Due to the dependence of bubble survival on plume effects, effectively modeling the relationship between methane generation in sediments and atmospheric emissions requires an understanding of the spatial and

temporal concentration of ebullition. At the spatial scale of meters and above, ebullition is often observed to be concentrated spatially into discrete seeps [*Greinert*, 2008; *Schneider von Deimling et al.*, 2010; *Walter Anthony and Anthony*, 2013; *Bayrakci et al.*, 2014; *Skarke et al.*, 2014]. However, at least in some settings, the spatial structure of distant methane vents is ephemeral. In a record of sonar-detected ebullition in Upper Mystic Lake (UML), MA, a characteristic spatial structure of apparently discrete seeps was observed over periods up to 1 day in duration, but over longer periods the occurrence of spatially independent venting made the pattern indistinguishable from a completely spatially random process [*Scandella et al.*, 2016]. Other studies on the UML, a dimictic, eutrophic kettle lake north of Boston, MA, include a 4 month record of ebullition from five surface-moored bubble traps that showed surprising synchronicity in hydrostatically triggered ebullition episodes, despite the sensors' being located over water depths ranging from 9 to 25 m [*Scandella et al.*, 2011; *Varadharajan and Hemond*, 2012; *Delwiche et al.*, 2015]. In contrast with this wealth of observations at the field scale, fine-scale observations of the spatial distribution of ebullition from natural sediments are lacking.

Understanding the mechanisms controlling bubble growth and mobility in soft sediments is another motivation for this work, as the physics of multiphase flow in deformable porous media is complex and an active area of research. The preferred mode of gas mobility through fine-grained organic sediments, such as those found in UML [*Spliethoff and Hemond*, 1996], is via deformation of the particles, as opposed to capillary entry through large pore throats in coarse sediments [*Jain and Juanes*, 2009]. Previous mechanistic modeling of bubble mobilization in the framework of linear elastic fracture mechanics [*Gardiner et al.*, 2003; *Boudreau et al.*, 2005; *Algar et al.*, 2011a, 2011b] led to the speculation that bubbles tend to form in and follow the rise paths of previously released bubbles due to partial healing of the fracture toughness (K_{IC}) of sediments [*Algar et al.*, 2011b]). We approach the mechanics from the perspective of plastic deformation, where the parameter setting the limit on effective stress under tension is the tensile strength, σ_T [*Scandella et al.*, 2011]. The mechanism of tensile strength reduction should support reuse of existing bubble conduits, diverting bubbles laterally to grow and rise toward existing outlets. Subvertical bubble rise has been observed in laboratory experiments in fine, uncompacted glass beads [*Kong et al.*, 2009] and gelatin [*Boudreau et al.*, 2005]. One way to evaluate the role of the strength reduction effect is to ask over what spatial scale does this reduced cohesion cause conduits to be reused in the context of laterally homogeneous methanogenesis? If preexisting conduits are significantly more favorable than undisturbed sediments, gas will be collected toward an outlet from a larger area, and the major outlets will show more distant spacing.

While the spacing of outlets is expected to be related to the magnitude of the drop in tensile strength, the persistence of outlets is expected to depend on the rate of recovery of tensile strength. Previous research on soft, fine-grained sediments has revealed recovery of the yield stress over the scale of months [*Merckelbach et al.*, 2002]. Mechanistically, this strengthening is explained as a result of decreasing distances between particles of neighboring aggregates during compaction, causing an increase in strength of van der Waals forces and hydrogen bonds [*Merckelbach*, 2000; *Merckelbach et al.*, 2002; *Holtz and Kovacs*, 2010]. We hypothesize that σ_T is temporarily reduced by bubble passage and recovers slowly with time until the next release, similar in concept with the state parameter in formulation of dynamic friction under shear mobilization of rock fractures [*Dieterich*, 1979; *Ruina*, 1983]. If tensile strength recovers slowly relative to the timescale of gas generation, as suggested by previous studies, then individual outlets may be expected to be reused over multiple cycles of gas generation and release, to persist over weeks or months.

Previous studies have investigated the flow paths from a point gas injection source to the sediment surface and found that bubbles escape at distant outlets due to subvertical migration during rise through migrating air channels [*Kong et al.*, 2009] in an expanding, parabolically shaped "fluidized zone" [*Varas et al.*, 2011; *Ramos et al.*, 2015]. The width of a bubble release channel network increases with time, though that process appears to reach a steady state over the scale of minutes to hours and again occurs with gas supplied through a needle [*Kong et al.*, 2009, 2010]. While the fluidized zone increases in area over time, the majority of gas flow remains focused through a central channel [*Ramos et al.*, 2015]. These experiments involved significant simplifications relative to natural lake sediments: a needle injection source at constant flow rates, larger grains (diameter >200 μm versus clay platelets of order 0.1–10 μm), and no cohesion. Given these sparse observations, it is unclear what morphology of the conduit network would arise in the context of laterally distributed methane, and how that morphology would develop over time. We hypothesized that the combination of tensile strength reduction and slow strength recovery would lead to outlets spaced at least 5–10 cm apart and that persisted in activity over the scale of weeks to months.

A number of experiments have investigated how air injection at a point can enhance pore water exchange [*Klein*, 2006; *Yuan et al.*, 2007], create surface features [*Varas et al.*, 2009], and create bubbles whose size depends on the injection rate and grain size [*Greinert and Nutzel*, 2004; *Meier et al.*, 2011]. However, no studies have observed the spatial distribution of bubble release points from incubated natural sediments. *Comas and Wright* [2012] observed bubbles released from methane-generating peat with a downward looking camera both in situ and in a laboratory sample, but their focus was on quantifying the temporal variability in ebullition, rather than understanding the spatial component of interest here. Interestingly, that study found a positive correlation between atmospheric pressure and the ebullitive flux, compared with the majority of studies, which find that ebullition is triggered by falling atmospheric pressure [*Mattson and Likens*, 1990; *Fechner-Levy and Hemond*, 1996; *Tokida et al.*, 2007; *Scandella et al.*, 2011; *Varadharajan and Hemond*, 2012; *Yvon-Durocher et al.*, 2014; *Scandella et al.*, 2016], among other factors. Further experiments on wetland sediments have demonstrated triggering of ebullition with ebbing and flowing tides but did not detect the release of individual bubbles or quantify the spatial variability in ebullition [*Chen and Slater*, 2016].

Here we present results from a laboratory incubation of sediments from Upper Mystic Lake (UML), MA, which show hydrostatic triggering and inhibition of ebullition, temporal clustering of ebullition events, and the degree of reuse of bubble outlets over minutes to months. Based on these results, we propose a conceptual model linking distributed methanogenesis to ebullition through discrete, persistent outlets.

2. Materials and Methods

2.1. Physical Apparatus and Initiation

The physical apparatus was designed to incubate natural sediments while permitting manipulation of the water level, visualization of the time and lateral location of bubble release from sediments, and collection of the emitted gas (Figure 1). The sediments were held in an acrylic tank with external dimensions $46 \times 46 \times 51$ cm ($18 \times 18 \times 20$ inches) and wall thickness of 6.35 mm ($\frac{1}{4}$ inch). An aluminum frame was mounted around the midline of the tank in order to constrain its expansion with pressurization and to mount the light strips for imaging.

The lateral distribution of methane ebullition may be controlled by a combination of transport processes and heterogeneity in the methane source, and we sought to minimize the latter influence by reconstituting the sediments. Sediments and hypolimnetic water were collected using an Ekman dredge from the deepwater basin of UML at 20 m water depth (43.4330°N, 71.1495°W), adjacent to the deployment locations of a multibeam sonar lander employed in a complementary field campaign [*Scandella et al.*, 2016]. Within this basin, the previously measured sediment accumulation rate of 0.5 cm/yr is expected to be homogeneous due to relatively flat bathymetry, and freeze cores from within the basin show strikingly similar depth profiles of arsenic concentration [*Spliethoff and Hemond*, 1996]. Approximately 90 L of dredged, watery sediments and 15 L of hypolimnetic water were slurried in a 208 L drum using a paint-mixing drill bit for 5 min, with the top of the drum sealed around the drill bit and headspace purged with nitrogen gas to minimize oxygenation. The reconstituted sediments were then transferred into the tank using a peristaltic pump over 8 h, which further pulverized any remaining small clumps of sediment and may have thereby liberated labile carbon. The tubing had an inner diameter of 9.5 mm (3.5 inches), and approximately 10 g of larger solid material (mainly leaves and sticks) did not fit and so was removed during the pumping process. While the sediments appeared to remain suspended during the filling process, the direction of the inlet tube was varied periodically to avoid preferentially loading any region of the tank or scouring away early-deposited sediments.

After the tank was filled, the sediments were allowed to settle and incubate at laboratory temperature (20–22°C) for 6 months prior to the experiments presented here. During that time, the tank was kept sealed for periods lasting up to 20 days. These periods limited the potential for infauna to survive, compounding earlier obstacles such as the increase in temperature and being pumped through a peristaltic pump. Over the initial incubation period, the sediments generated and released more than 3 L of gas. The level of the sediments was 26 cm above the bottom of the tank after filling, and it compacted to 24 cm within 1 month and 22 cm after 17 months.

The water level was maintained above the top of the tank using an external reservoir, and the pressure could be dropped to trigger ebullition by raising and lowering the reservoir. The rate of change of water level was limited to ~1 cm/min to avoid creating significant fluid flow into or out of the tank, which expanded or contracted by ≈12 mL/cm change in water level. Ebullition was observed during five experiments that were

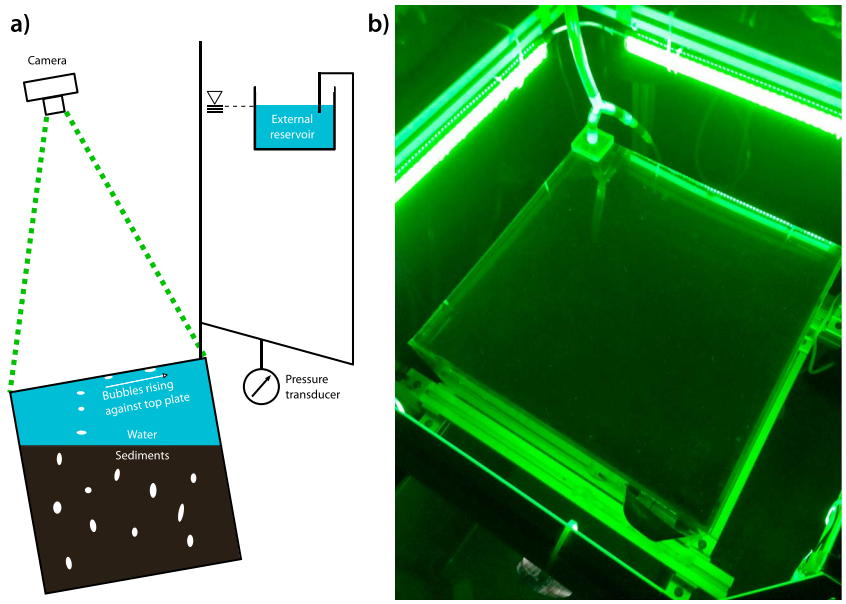

Figure 1. (a) Diagram of the sediment incubation setup. Bubbles escaped from the sediments, rose through the water column, hit the top plate, and slid to the upper corner. At the corner, they escaped through an outlet tube that was large enough (9.525 mm internal diameter) to permit them to rise into the outlet column for collection (when the outlet was closed at the top and filled with water) or to a fume hood. The water level was maintained above the top of the tank with an external reservoir, and the pressure was measured with a transducer attached to the plumbing. (b) Image of the tank setup from an oblique view above. Light was provided by eight LED light strips covered with green filters to minimize potential to promote photosynthesis, and the tank was restrained at midheight with an aluminum frame of 80/20®. The outlet tube is visible at the upslope corner.

conducted over a period of 10 months between May 2015 and February 2016 and that lasted between 4 and 17 days (Table 1). Experiments 1, 2, and 4 were triggered by drops in the water level, and Experiment 1 was also subjected to an increase in water level. Experiments 3 and 5 were observed under ambient conditions.

Gas bubbles released from the sediments would rise through the overlying water, impact against the top plate, and slide toward the upslope corner due to a 9° tilt in the tank, in order to maintain a mostly bubble-free surface to detect subsequent bubble arrivals. From the upslope corner, bubbles would rise through an outlet tube, in which they could be collected or vented into a fume hood. The distance bubbles traveled through water from the sediment surface to the tank top was limited to ≈20 cm, so bubble dissolution played a negligible role [*McGinnis et al.*, 2006].

The water level was recorded at 20 Hz using a Honeywell pressure transducer (24PCAF6D) and Dataq analog-digital converter, and the barometric pressure was recorded using a Solinst Levelogger at 5 min intervals. The tank was lit from above on all sides with 8 LED light strips (2700K color temperature, 18 inches long, and 5.9 W each), which were covered by green filters to minimize the potential to promote photosynthesis. The system was housed in a darkroom to keep out external light for the sake of consistent imaging and inhibition of photosynthesis. Images were captured using an Allied Vision Technologies "Pike" scientific camera, mounted with a 25 mm f/1.4 lens. The camera was oriented horizontally, with the image reflected off of a

Table 1. Summary of Imposed Water Level Perturbations and Fluxes for the Five Experiments: Duration, Mean Flux, and Magnitudes of Increase and Decrease in Water Level, and R^2 of 2 h Flux Versus Hydrostatic Pressure (With the Sign of R)

Experiment #	Start Date	Duration (days)	Mean Flux (mL m^{-2} d^{-1})	Water Level Increase (cm)	Water Level Decrease (cm)	R^2
1	5 May 2015	17	400	64	60	(−) 0.02
2	17 Jun 2015	15	900	0	68	(+) 0.004
3	10 Jul 2015	7	700	0	0	(−) 0.32
4	10 Sep 2015	4	2000	0	67	(+) 0.23
5	12 Feb 2016	14	400	0	0	(−) 0.34

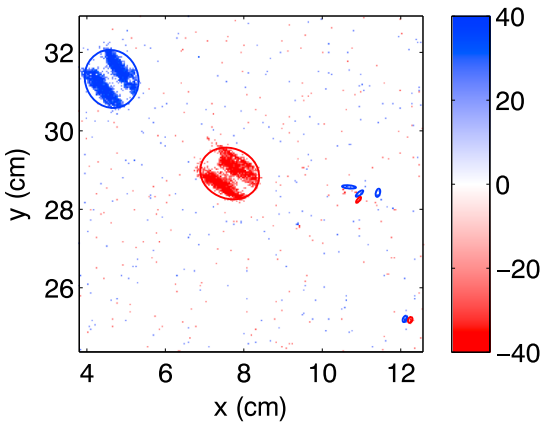

Figure 2. Example of segmented image differences, with increases in brightness in blue and decreases in brightness in red. Clusters of pixels were identified with the DBSCAN algorithm [*Daszykowski et al.*, 2001], and the best fit ellipse for each cluster was used to estimate the bubble area.

tilted mirror, to accommodate the narrow angle of view of the lens within the height of the room. The tilt of the camera and mirror was set with a frame of aluminum 80/20. The camera was controlled using MATLAB to acquire images at a rate of 3 times per second, with a resolution of 1200 × 960 pixels and 8 bit greyscale depth.

2.2. Image Processing

Bubbles were identified automatically from images of the top of the tank in order to estimate their location and time of release, as well as their volume. Due to the mild slope and partial wetting of the acrylic tank surface, small bubbles tended to become immobilized against the tank top so that a population of many small bubbles appeared in any given image. The areal density and wide range of bubble sizes, random pixel noise from the camera, and relatively low resolution (0.4 mm) made it impossible to segment the individual images reliably. This fact, combined with the large population of bubbles that would have to be matched between successive images, made traditional particle-tracking algorithms impractical for analyzing the images.

However, because only location and time of bubble arrival against the top plate were relevant for analysis, tracking the motion of bubbles toward the outlet was not necessary. Instead, we found that new arrivals could reliably be detected and distinguished from bubble motion by analyzing *differences* between successive images. Bubbles appeared as bright patches, so arrival of a bubble caused the brightness to increase, and disappearance of a bubble caused the brightness to decrease. The patches of increase and decrease in brightness were typically very sparse and distinguishable from the noise for bubbles larger than 1 mm in diameter. They were therefore readily identified using a clustering algorithm. In the case of bubble motion, a downslope decrease in brightness (disappearance) could be matched with an upslope increase in brightness (arrival), if the transition obeyed physically based limitations on its speed, direction of motion, and fractional change in area.

The method proceeded as follows and is illustrated in Figure 2:

1. Subtract successive images to detect increases or decreases in brightness.
2. Separate increases in brightness (appearances) from decreases (disappearances), and for each, the next steps are taken.
3. Threshold the difference to find active pixels. For the setup described here, a threshold of 20 (out of 255 for 8 bit images) was used.
4. Identify bubbles by clustering using density-based scanning (DBSCAN) [*Daszykowski et al.*, 2001], clusters of at least 5 pixels within a maximum separation of 3 pixels between any two. For the spatial resolution of 0.4 mm used here, this sets a minimum detectable bubble diameter of ≈1 mm.
5. For each identified cluster, classify it as a new bubble arrival or motion of an existing bubble.

Bubbles were classified as new arrivals only if there were no disappearances downslope with consistent speed, direction, speed perpendicular to the upslope direction, and fractional change in area. Differences over four successive observations (≈1.3 s) were searched to find potential motion matches. The determination of whether a pair of opposite-polarity changes (appearances and disappearances) could feasibly represent bubble motion was determined with a scoring system based on physically based aspects of the putative motion (speed, direction, cross-slope speed, and fractional change in area). The scoring parameters were tuned empirically using a training data set of 1014 manually classified changes (31 new arrivals, with the remainder due to bubble motion).

The 5 pixel minimum cluster size was effective at rejecting noise from the image differences, but it also caused spurious identification of many arrivals of small bubbles. This is because bubbles smaller than 1.5 mm in

diameter frequently did not show above-threshold activity in 5 or more pixels. When a small bubble moving against the top was identified by its upslope increase in brightness between images, but not by its downslope decrease in brightness, it could be mistakenly identified as a new bubble arrival rather than bubble motion. The choice to search for potential matches over four successive observations ameliorated this effect but did not eliminate it. The estimated number of bubble arrivals was highly sensitive to the minimum cluster size, as reducing the minimum size from 5 pixels to 4 introduced 40% more putative bubble arrivals. However, these additional bubbles only increased the total volume identified by 1%, demonstrating that volume estimates with this method are significantly more reliable than bubble counts. Therefore, all statistics used in the following analysis were weighted by each bubble's volume.

2.2.1. Estimation of Bubble Volume From Area

The volume of individual gas bubbles was estimated assuming that bubbles adopt a static shape against the top plate. Bubbles with contact area smaller than the capillary length ($\kappa^{-1} = \sqrt{\gamma/\Delta\rho g}$) take the shape of a spherical cap, and larger bubbles spread into a pancake shape with thickness $h = 2\kappa^{-1}\sin(\theta/2)$ (*Queré* [2005], see Figure 3a for a schematic and definition of the different variables). When the Bond number, Bo $= (r\kappa)^2$, is in the range of 1 and for $\theta > 60°$, the bubble shape may be approximated as an ellipsoidal cap [*Lubarda and Talke*, 2011]. For an interfacial tension of 70 mN/m between methane and water [*Schmidt et al.*, 2007] and contact angle of 70° for air and water on an acrylic surface [*Osti et al.*, 2009], it was found that the ellipsoidal model represented the bubble area-volume relationship not only in the transition between large and small bubbles but also in the limits (Figure 3b). Therefore, the ellipsoidal model was used to estimate all bubble volumes.

Because bubbles did not assume their equilibrium shape instantly, and because bubbles were sometimes imaged even before they hit the top of the tank, the initial bubble area tended to underestimate the equilibrium area. To compensate for this effect, the area of a bubble was measured using the last image that was matched with the initial arrival by bubble motion.

2.3. Gas Volume and Content Measurement

A validation experiment was conducted in which the volume of gas released was estimated using both the automated image analysis and by collecting the gas that escaped from the tank. Gas was collected periodically at the top of a water-filled tube and stored in glass syringes within 24 h of release from the sediments. Gas sample volumes were measured using glass syringes, and the chemical composition was analyzed on a F&M gas chromatograph (GC) with a Molecular Sieve 5a column (which can separate and elute CH_4, N_2, and O_2 but not CO_2) and a thermal conductivity detector. The GC was calibrated using methane standards of 0%, 10%, 50%, and 100%, and the measured responses fit calibration lines with $R^2 \geq 0.9968$ (see supporting information, SI).

2.3.1. Estimation of Fluxes

Bubble arrivals were binned into fluxes on a regular 1 cm resolution spatial grid (see SI) and at regular intervals in time. The image collection system was occasionally nonoperational, and for time intervals where the system was nonoperational for less than 50% of that interval, the flux was extrapolated in time to cover the entire interval. When the nonoperation was longer than 50% of the time interval, the data were not used in calculating the flux.

The spatial distribution of ebullition was expected to be influenced by the edges of the tank, due to the tilted orientation of the tank and the influence of walls. Thus, data from within 4 cm of any edge of the tank were not analyzed, and data were only plotted from coordinates 4–41 cm in both directions.

2.4. Statistics for Temporal and Spatial Clustering

2.4.1. Hazard Function

The temporal relationship between successive bubble releases can be characterized by the distribution of interarrival times, τ. Events that occur independently in time may be modeled as a Poisson process, and temporal clustering or regularity may be detected as deviations of the probability density function $f(\tau)$ from that expected from a Poisson process. Especially useful for making this comparison is the hazard function, $h(\tau)$, which quantifies the probability of an event occurring, conditioned on a given amount of time having passed since the last event:

$$h(\tau) = \frac{f(\tau)}{1 - F(\tau)}, \tag{1}$$

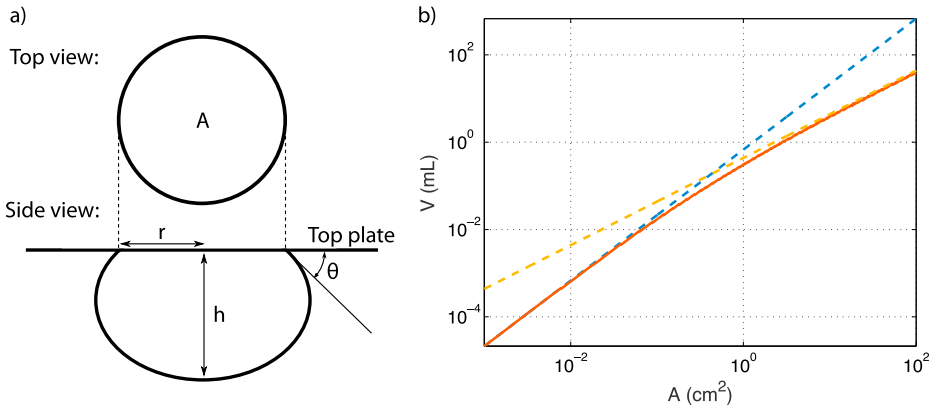

Figure 3. (a) Diagram showing the relationship between apparent bubble area A against the top plate (from above) and its height h, radius r, and contact angle θ (from the side). (b) Models showing bubble volume versus apparent area for spherical caps (blue dashed), ellipsoidal caps (dashed), and puddles (yellow dashed). The ellipsoidal cap model was used for all bubble sizes in this study because it asymptotically approaches the two other models in the limit of large and small bubble sizes observed in the tank.

where $F(\tau)$ is the cumulative density function (CDF) [*Stapelberg*, 2009]. For a Poisson process, events are independent and have uniform probability, corresponding to constant h since the events have no memory of previous arrivals. For a Weibull process—a model often used in reliability engineering to model component failures—the hazard function is a power law, $h(\tau) = (\beta/\lambda)(\tau/\lambda)^{\beta-1}$, where β and λ are the shape and scale parameters, respectively. A decreasing power law ($\beta < 1$) corresponds to strong temporal clustering, while an increasing power law ($\beta > 1$) is associated with more regularly periodic arrivals [*Stapelberg*, 2009].

For the analysis presented here, each bubble's contribution to h is weighted by its volume, so that $h(\tau)$ properly represents the rate of volume flow per the volume not yet released after τ. This was important for the analysis of our experiments because the method of matching image changes to identify bubble motion (as opposed to arrival of a new bubble) was poor for bubbles smaller than ≈1.1 mm (or 3 pixels) in diameter, meaning that small, moving bubbles could create the appearance of more frequent arrivals.

The hazard function for a spatiotemporal point process such as bubble escape depends on the spatial scale over which it is measured. Bubble releases detected within a larger spatial observation window typically occur more frequently than they do within a smaller window, and the magnitude of the hazard function is larger. However, it is the *slope* of the hazard function that reflects temporal (in)dependence of successive events. For the analysis shown here, we compare the hazard function measured for events within square observation windows of both 3 cm and 37 cm on a side, where the fine-resolution scale reflects the width of discrete, high-activity outlets.

2.4.2. Radial Distribution Function

We analyze the size, intensity, spacing, and persistence of spatial clusters using the radial distribution function (RDF), which quantifies the degree of spatial concentration of events at a given distance from other events, relative to a completely spatially random (CSR) process. We estimate $g(r)$ using the marked pair correlation function [*Ohser and Mücklich*, 2000; *Illian et al.*, 2008],

$$g(r) = \frac{1}{2\pi r \lambda^2 \hat{A}(r)} \sum_{x_1, x_2 \in W}^{\neq} m(x_1) m(x_2) k(||x_1 - x_2|| - r), \tag{2}$$

where λ is the areal mass density, $\hat{A}(r)$ is the isotropized set covariance of the observation area at distance r, $m(x_i)$ is the mark or intensity associated with point x_i (here the bubble volume), and k is a box kernel with bandwidth $h = 1$ cm. Values of $g(r) > 1$ indicate spatial clustering at interpoint distance r, while values $g < 1$ indicate spacing or regularity, a lower-than-expected density of points at range r.

Another tool for investigating the fine-resolution spatiotemporal relationship between bubbling events is the spatiotemporal radial distribution function (ST-RDF). This statistic extends the concept of the RDF $g(r)$ into time with the introduction of time lags u between events, so that $g(r, u)$ is the amount of activity within the

ring of radius r around an event and following it by time lag u. The metric is computationally intensive to estimate over long-duration samples required to investigate large u, but for short times it can confirm the presence of spatiotemporal clustering more precisely than using the RDF over short time intervals.

3. Results

The methods presented above enabled a wide variety of observations about the nature of ebullition from natural, reconstituted sediments. Below we present chemical analysis of the released gas, evaluation of the accuracy of the image analysis method, estimation of the bubble size distribution, and characterization of the temporal and spatial variability in methane fluxes. Ebullition was observed during five experiments that were conducted over a period of 10 months between May 2015 and February 2016 and that lasted between 4 and 17 days (Table 1).

3.1. Gas Composition and Flux Magnitudes

3.1.1. Gas Composition

Gas samples from Experiment 5 were 83 ± 5% methane by mass ($n = 7$ after rejecting one sample that failed Dixon's Q test at 99% confidence for both methane and nitrogen concentrations, suggesting contamination by air during sampling). The nitrogen concentrations were 8 ± 4% and may have either come from the sediments or exsolved into the gas phase from the water in the collection tube, which was sparged with nitrogen to remove oxygen. Trace amounts of oxygen were detected but not quantified (see SI).

3.1.2. Flux Validation Results

To test the accuracy of the automated image analysis, the volume of gas released during Experiment 5 was collected over 14 time periods of duration 6–42 h and compared against volume estimates from the image analysis over the same periods. The volumes collected matched those estimated by image analysis within 16 ± 8% (mean relative absolute error ±1 standard deviation). The best fit line had a slope of 1.04 and $R^2 = 0.983$ ($n = 14$), showing that the bias in the image analysis method is limited to ≈5%. When the volumes were normalized by their sampling intervals to estimate fluxes, the best fit line had a slope of 1.05 and $R^2 = 0.975$ ($n = 14$, Figure 4a).

The uncertainty associated with flux estimates depends on the number of bubbles that arrive during a given observation period, because unbiased noise in the measurements will tend to average toward zero by the central limit theorem. The validation experiment showed that, in the limit of many bubbles when measurement noise may be neglected, the bias (and thus uncertainty) is limited to ≈5%. Over shorter measurement periods, on the scale of seconds to minutes, however, the bias in estimated bubble volumes and fluxes may be higher.

3.1.3. Flux Magnitudes

The long-term spatiotemporal average flux of all experiments was approximately 0.06 mL cm^{-2} d^{-1} or 600 mL m^{-2} d^{-1}. The only source of organic matter for the experiment was introduced at the beginning of the incubation, so we expected that ebullition rates would drop as the finite carbon source was gradually depleted over the course of the incubation. While there was substantial variability in mean flux between the experiments (Table 1, standard deviation = 600 mL m^{-2} d^{-1}), no decreasing trend was observed (one-tailed Kendall rank correlation test, $p = 0.6$). The total amount of methane-derived carbon emitted over 15 months between initiation and the final experiment, ≈0.04 kg C, was small compared with the ≈4 kg of organic carbon content of the sediments (conservatively assuming 90% porosity and 20% organic carbon content, based on previous measurements of UML sediments [*Spliethoff and Hemond*, 1996; *Varadharajan*, 2009]).

3.1.4. Bubble Size Distributions

The distribution of bubble sizes estimated using the ellipsoidal cap method yields a distribution dominated numerically by bubbles smaller than 2 mm in diameter (Figure 4b). However, as described above, counts of these small bubbles are not as well constrained as the volume estimates. Although these bubbles constitute 79% of the bubbles by number, they contribute only 3.3% of the total volume released. The frequency of such small bubbles is large compared with other in-field estimates of the BSD in UML, which found <1% smaller than 2 mm in diameter [*Delwiche et al.*, 2015]. Part of that discrepancy may be attributed to a lower detection limit for bubble sizes for the instrument used in that study, as bubbles smaller than 2 mm in diameter were not tested in the calibration of the device, and it is also likely that many of the small bubbles were spuriously detected by our method. To minimize the impact of these potential artifacts on the results, the following analysis was carried out with volume-weighted statistics (section 2.4).

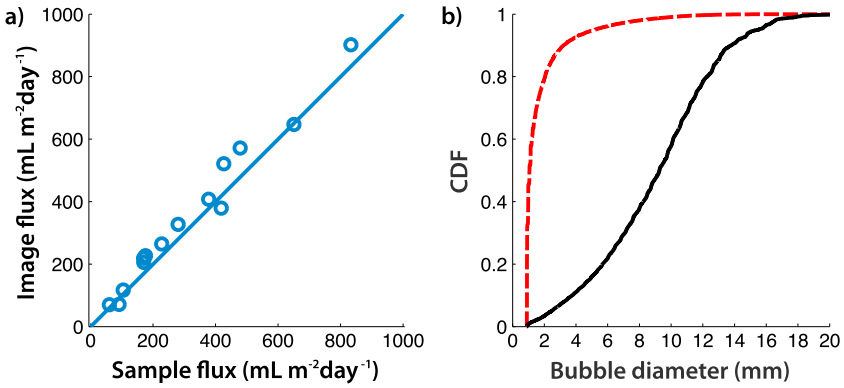

Figure 4. (a) Comparison of gas fluxes measured with sampling of gas and image analysis shows strong predictive ability ($R^2 = 0.975$). The shown 1:1 line is close to the slopes of best fit line, 1.05. (b) CDF of bubble diameters (red dashed line) shows a population predominance of small bubbles, with those less than 2 mm comprising 79% of the bubbles by number. The small bubbles have minor impact on volume-weighted CDF (black solid line), constituting 3.3% of the total volume released.

3.2. Episodicity of Methane Venting

3.2.1. Hydrostatic Control of Ebullition

The five experiments reported here were conducted under different conditions of hydrostatic pressure control: Experiments 1, 2, and 4 were forced by large drops in hydrostatic pressure, Experiment 1 included a period of raised hydrostatic pressure, and Experiments 3 and 5 were left to respond to barometric pressure variations (Table 1).

Experiment 1 was carried out in three phases of water level control: an initial period of low water level until 7 May 2015, an intermediate period of raised water level until 10 May, and a final period with low water level again (Figure 5). Prior to the experiment, the water level had been lowered by 45 cm on 1 May 2015, and in the week before that the level was cycled down and up by 38 cm. These perturbations were large and frequent relative to those observed in the water level of Upper Mystic Lake [*Scandella et al.*, 2011]. While the preexperimental ebullition was not observed with the video system, a rough estimate based on the change in volume of the contents of the tank suggests that ~600 mL of gas was released during the 12 day period preceding Experiment 1, corresponding to a flux of ~0.03 mL cm^{-2} d^{-1}, which was typical for low-flux periods from the tank.

During the initial phase of Experiment 1, the flux remained relatively low, rising only to about 0.2 mL cm^{-2} d^{-1}. After the water level was raised by 64 cm, the flux dropped below 0.01 mL cm^{-2} d^{-1} within 1 day and remained that low until the water level was dropped again on 10 May. With the resumption of low-pressure conditions, the flux immediately jumped back up to above 0.1 mL cm^{-2} d^{-1} and peaked to above 0.4 mL cm^{-2} d^{-1} on 11 May. For the remainder of the experiment, the water level was maintained while barometric pressure variations caused the pressure to dip by ≈20 cm on 12–13 May and again from 19 to 21 May. Following the initial peak on 11 May, the flux grew gradually from 13 to 15 May, culminating in an ebullition event that was so vigorous that it suspended sediments that became temporarily adhered to the top of the tank and significantly occluded the camera's view of rising bubbles. The period from 11:40 A.M. to 11:00 P.M. on 15 May was excluded from the data analysis because the images could not be reliably analyzed to identify the arrival location and time of bubbles. Following this period of intense activity and after the sediment had detached from the tank top, the flux was maintained at below 0.1 mL cm^{-2} d^{-1} for the remainder of the experiment, even during the pressure drop from 18 to 19 May.

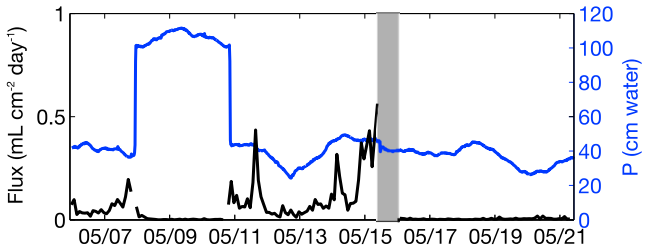

Figure 5. Time series of flux and hydrostatic pressure for Experiment 1. The gray bar from 11:40 A.M. to 11:00 P.M. on 15 May represents a period of vigorous venting (shaded light gray) when the data were unusable because suspended sediment became attached to the regions on the top of the tank and occluded the view of arriving bubbles.

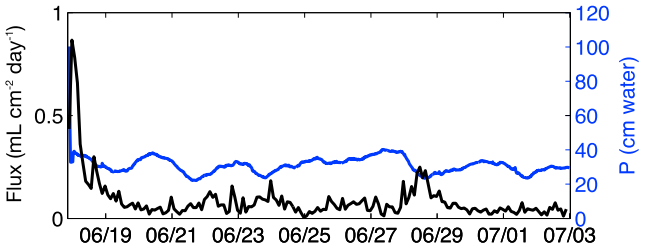

Figure 6. Time series of flux and hydrostatic pressure for Experiment 2.

Experiment 2 was driven by a 68 cm drop in water level on 17 June, following a 27 day period where the water level was maintained at a high level intended to inhibit ebullition while sediments recharged their gas contents (Figure 6). After the water level was lowered, it was maintained for the remainder of the experiment so that pressure changes reflect barometric changes, which were of magnitude ≈20 cm. The gas flux peaked within 2 h of the drop in hydrostatic pressure and then decayed to the background rate over the following 3 days. For the remainder of the experiment, the gas flux remained below 0.25 mL cm^{-2} d^{-1} but showed minor peaks during three periods of low hydrostatic pressure.

Experiment 3 was carried out at a constant water level following an extended period at that same low level imposed during Experiment 2 (Figure 7). The gas flux remained below 0.25 mL cm^{-2} d^{-1} but showed a consistent, slow increase over a multiday drop in hydrostatic pressure from 13 to 15 July and then a decrease as the hydrostatic pressure rose again.

Experiment 4 was carried out under similar conditions to Experiment 2, beginning with a 67 cm drop in water level and then leaving the level constant for the remainder of the experiment (Figure 8). The gas flux peaked at 0.7 mL cm^{-2} d^{-1} immediately and decayed over the following day to a roughly constant level ≈0.1 mL cm^{-2} d^{-1}.

Experiment 5, like Experiment 3, was carried out at a constant water level and following an extended period at that same level (Figure 9). The barometrically driven pressure variations were of a larger magnitude (50 cm vs 20 cm), but the magnitude of the fluxes showed a similar response to Experiments 2 and 3, peaking at 0.2 mL cm^{-2} d^{-1} at the lowest hydrostatic pressures.

3.2.2. Temporal Clustering

The temporal relationship between successive bubble releases was analyzed using the hazard function, $h(\tau)$, where decreasing power law in $h(\tau)$ corresponds to strong temporal clustering, while an increasing power law is associated with more regularly periodic arrivals [*Stapelberg*, 2009]. For the combination of all experiments, $h(\tau)$ for 3 cm pixels shows power law decay with slope -0.4 ± 0.1, consistent with a Weibull process with $\beta = 0.6 \pm 0.1$ (Figure 10). For coarse pixels (the entire area), h also decays as a power law with slope -0.4 for $\tau < 2$ min and then decays more rapidly.

Comparing the hazard function among the five experiments yields some insight into the relationship between hydrostatic triggering and temporal clustering (Figure 11). Experiments 1, 2, 4, and 5 are qualitatively similar, except for a dip in the hazard for coarse pixels in Experiment 1 from ≈5–15 min, indicating that temporal clustering tended to occur over interarrival times shorter than 5 min over the entire tank area. The rebound of h around $\tau = 60$ min in Experiment 1 suggests relative regularity of arrivals at this timescale, though the small number of long interarrival times makes estimates of $h(\tau)$ less certain over long timescales.

Compared with Experiment 1, Experiment 2 shows slightly shallower decay in its coarse h, indicating a slightly stronger role for independent arrivals over dependent triggering. Experiment 3 shows near-Poisson behavior of the coarse pixels, as well as of fine pixels when $\tau \geq 1$ min, suggesting that the bubble releases were relatively independent and not self-sustaining. The temporal independence in Experiment 3 may be related to the depletion of the stored gas during Experiment 2. However, Experiment 4 also displayed shallower decay in h for both coarse and fine pixels for $\tau \geq 1$ min, and that experiment was carried out without a preceding experiment that would deplete it, and it showed a strong flux response to the hydrostatic pressure drop.

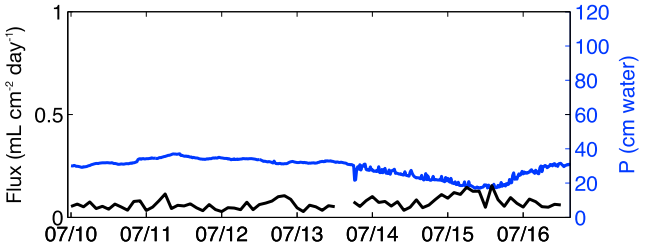

Figure 7. Time series of flux and hydrostatic pressure for Experiment 3.

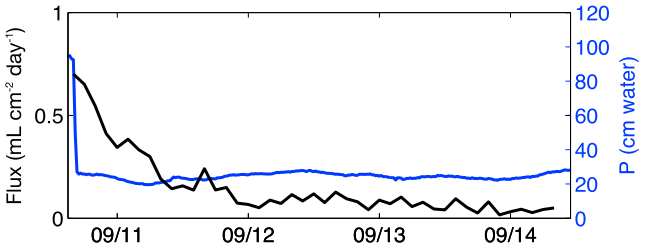

Figure 8. Time series of flux and hydrostatic pressure for Experiment 4.

The maximum observable τ is limited by the duration of the uninterrupted periods of image collection, whose histogram reflects the fact that only 17 periods lasted longer than 1 day (Figure 12). The imaging was interrupted by sample collection, cleaning of the imaging surface, switching hard drives for recording images, or any change in light away from the tank indicating the darkroom had been opened. Future experimental design efforts should aim to minimize these breaks in data collection, to enable analysis of long interarrival times.

3.3. Spatial Heterogeneity of Methane Venting

3.3.1. Gridded Flux Maps

The spatial distribution of fluxes varied significantly among experiments. For Experiments 1 and 2, the composite flux map over the experiment shows approximately 10 clusters of connected pixels with the highest fluxes, each spanning 2–5 pixels in diameter (Figure 13). Experiment 3 shows a few pixels with high flux, but they do not exhibit the degree of connection and spatial order evident in the first two experiments. Experiment 4 also shows connected clusters with high fluxes, but they are much more numerous and more densely spaced. Experiment 5 shows lower fluxes overall and much less spatial heterogeneity, though some of that appearance arises from the use of the same color scale for all subfigures.

The patterns of ebullition may be simplified and compared between experiments by automatically defining the major active outlets for each experiment. Outlets were defined as clusters of adjacent pixels each with flux above the 95th percentile of activity for that experiment (Table 2). Consistent with the qualitative observation from the composite flux maps (Figure 13), Experiments 1 and 2 had significantly fewer outlets and therefore larger characteristic spacing between the outlets than the later three experiments. The outlets still released a similar fraction of the total gas flux (≥34%) compared with the overall range (27–39%).

3.3.2. Temporal Variability Within Experiments

Within each experiment, the spatial pattern of ebullition showed variability over the scale of days. Within a given day for Experiments 1 and 2, the spatial pattern was dominated by 5–10 clusters of connected pixels, each 2–5 cm in diameter (Figures 14 and 15). During Experiment 1, there is repeated use of multiple outlets ~5 cm up and left from the center of the tank, as well as repeated use of an outlet in the bottom-left corner. During Experiment 2, the outlet just up and to the right of the center becomes active on day 1 and is reused on days 5–8 and 9–11. The rest of the outlets appear to go dormant after the initial high-flux period.

For Experiments 3, 4, and 5, the daily venting was more spatially distributed, with 20–100 clusters of active pixels contributing most of the flux (which was <6 mL cm^{-2} d^{-1}, small compared with the up to 25 mL cm^{-2} d^{-1} within the active pixels during Experiments 1 and 2) (Figures 16–18). It is difficult to ascertain reuse of such dense, small features across days from this calendar view, so we analyze the spatial clustering and its persistence statistically with the radial distribution function.

3.3.3. Spatial Clustering

We analyze the size, intensity, spacing, and persistence of spatial clusters using the radial distribution function, $g(r)$, where values of $g(r) > 1$ indicate spatial clustering at interpoint distance r, while values $g < 1$ indicate spacing or regularity, a lower-than-expected density of points at range r. The results from all five experiments show short-range clustering and long-range spacing, which appears as decay of $g(r)$, with $g > 1$ for $r < r^*$ and $g < 1$ for $r > r^*$, and where r^* is the crossover distance (Figure 19). We estimate $g(r)$ for spatial point patterns collected over time intervals of different durations, from 0.25 h to 48 h, and in all cases the magnitude of g was larger for short-duration intervals and

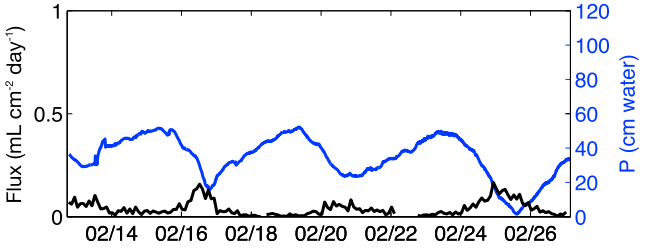

Figure 9. Time series of flux and hydrostatic pressure for Experiment 5.

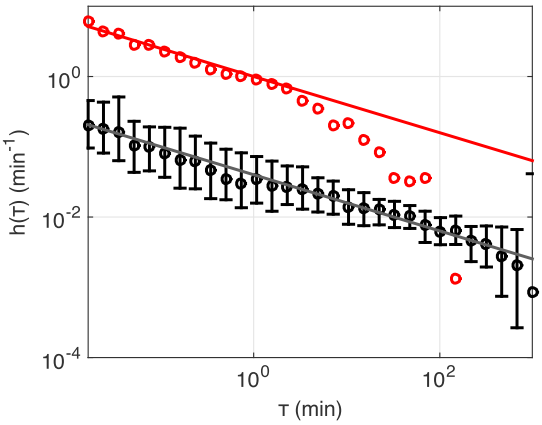

Figure 10. Hazard function over all experiments at two different spatial resolutions (3 cm, black and 37 cm, red). For the fine-resolution pixels, $h(\tau)$ shows power law decay with a slope of −0.4 (gray line). Within the interquartile range across pixels (black bars), the decay can be fit by a power law of slopes between −0.3 and −0.5 (not shown). This decay is consistent with temporal clustering from a Weibull process, with $\beta = 0.6 \pm 0.1$. For the coarse-resolution data (over the entire viewing area), h shows power law decay with slope −0.4 (red line) for $\tau \leq 2$ min and then a faster decay. The larger magnitude is due to the increased rate of arrival over the larger observation area.

decreased toward the signature of a spatially homogeneous process, $g = 1$, with increasingly long intervals. The decrease in magnitude of the signature of spatial organization shows a growing influence of spatially independent events over progressively longer timescales.

Although all experiments follow the same general trends in space and time, they differ in the crossover distance r^* and the timescale over which the spatial signal decays. Experiments 1 and 2 show strong short-range clustering, although the clusters are larger in size in Experiment 2 ($g > 1$ for $r \leq 6$ for 0.25 h samples in Experiment 1 and for $r < 3$ over the same duration in Experiment 2). Beyond that range, both show spacing of activity with $g < 1$. For progressively longer-duration samples, the strength of clustering and spacing decays roughly monotonically, except that the size of the clusters increases with time up to 10 cm in Experiment 1 and 7 cm in Experiment 2. Even over 48 h, the spatial clusters still remain strong with $g > 3$ at $r = 1$ cm, and this is consistent with the visible role of clusters in the composite maps for these experiments (Figure 13).

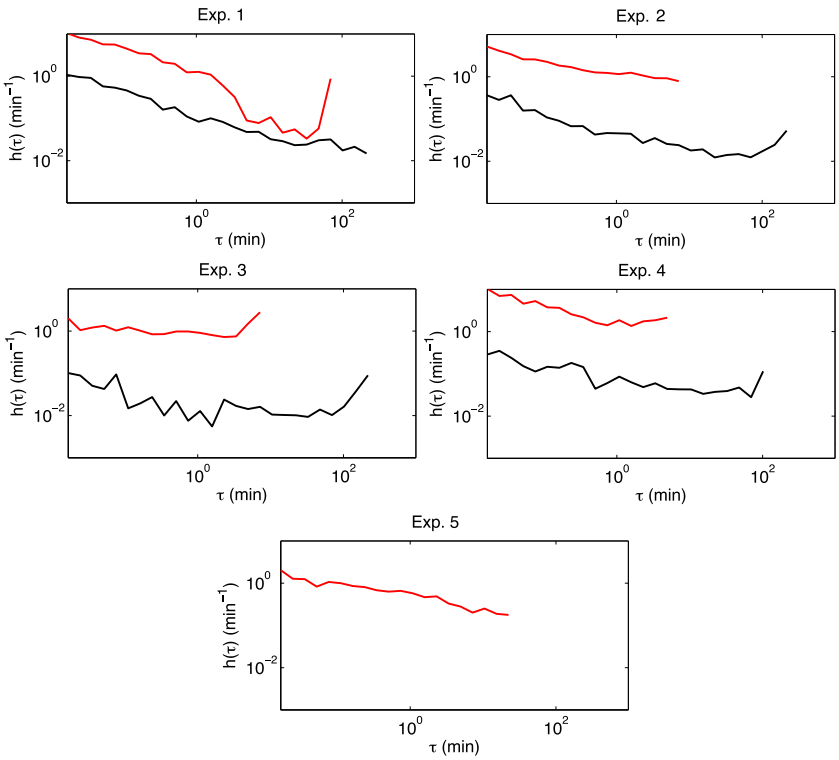

Figure 11. Hazard function for Experiments 1 through 5. Red lines for the entire observation area and black lines for 3 cm pixels.

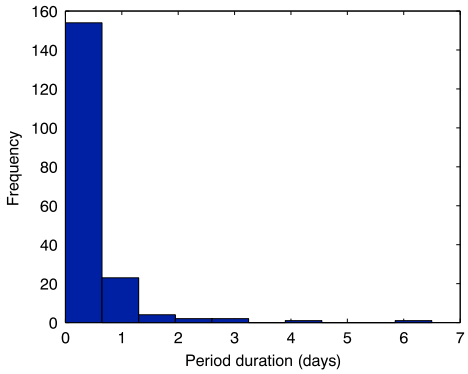

Figure 12. Histogram of durations of continuous periods of image collection shows that the majority of continuous periods lasted <1 day.

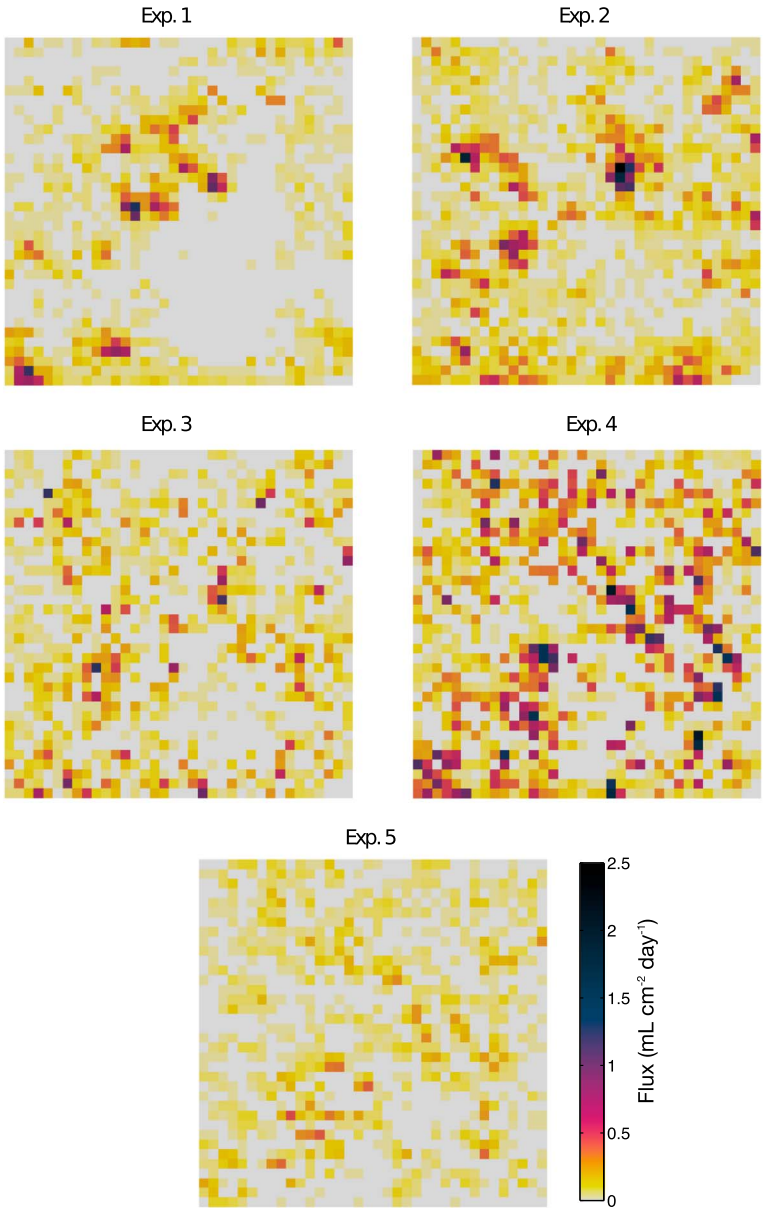

Figure 13. Composite flux maps from each of the five experiments.

Table 2. Summary of the Role of Major Outlets Identified for Each of the Five Experiments, Including the Number of Outlets, the Characteristic Spacing Between Them ($\rho^{-1/2}$, Where ρ Is the Number of Points Per Area), and the Fraction of the Volume Flux for the Experiment That Was Release Through Those Outlets

Experiment #	Number of Outlets	Characteristic Spacing (cm)	Flux Fraction (%)
1	19	8.5	39
2	28	7.0	34
3	54	5.1	37
4	43	5.6	32
5	45	5.5	27

Experiments 3–5 also show short-range clustering and long-range spacing over short duration samples, but the crossover range is shorter and roughly constant, and the strength of the spatial signature decays more completely with longer samples. The crossover range r^* for 0.25 h samples is between 2.5 and 4 cm, and with longer samples it does not appear to increase significantly (except in Experiment 5, where it may rise to 6 cm). The shorter crossover distance between clustering and spacing in the RDF for Experiments 3–5 than for Experiments 1 and 2 is consistent with the qualitative observation of a more significant role for large, distant outlets in the first two experiments (Figure 13). The RDF also decays toward 1 over longer samples, with $0.9 < g < 2$for samples longer than 1 day.

3.3.4. Spatiotemporal Clustering

The fine-resolution spatiotemporal relationship between bubbling events was investigated with the spatiotemporal RDF (ST-RDF). For Experiment 1, the ST-RDF showed clustering typically strongest for $r \leq 3$ cm and $\tau \leq 2$ min (Figure 20). The spatial scale matches the observed RDF for Experiment 1, but the temporal scale is much smaller than that of the RDF for temporally combined samples up to 1 day. The fact that the spatial clustering appears to dissipate faster indicates that most of the activity happens within a relatively short amount of time, even though the presence of the spatial clusters continues to dominate for long after. In a sense, the ST-RDF indicates the timescale of clustered activity, while the comparison of RDFs for samples of different durations (Figure 19) indicates the timescale for declustering, when the clustered signal becomes overwhelmed by spatiotemporally independent events.

3.3.5. Persistence of Dominant Outlets

The RDF shows that spatial clustering of ebullition can persist for multiple days within an experiment, but it is also possible to explore the persistence of major bubble outlets over the scale of weeks to months across multiple experiments by plotting these outlets for all experiments on the same axes (Figure 21). The map shows some locations of apparently enhanced activity, and the RDF confirms that the mild short-range spatial clustering is nonetheless significant for $r < 2$ cm and $r \approx 4$ cm when compared with the 95% confidence bounds for a CSR process (Figure 22, CSR simulated with 500 Monte Carlo replicates [*Wiegand and Moloney*, 22]). Therefore, major outlets show mild but significant reuse over the scale of months.

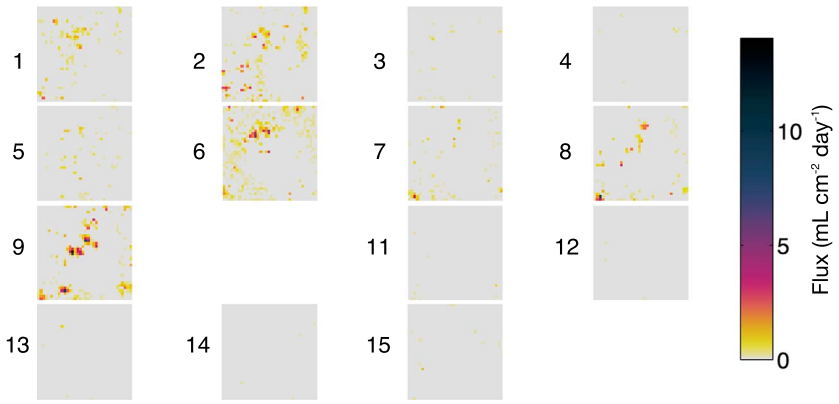

Figure 14. Calendar of daily ebullitive flux maps from Experiment 1, from 5 to 21 May 2015. Each square is 37 cm on a side with resolution of 1 cm. Day-long samples do not start at midnight and are not shown if the images were being collected during <50% of the period.

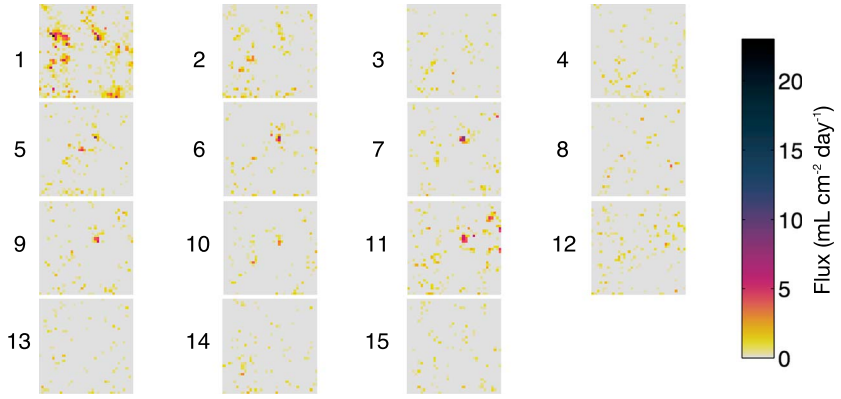

Figure 15. Calendar of daily ebullitive flux maps from Experiment 2, from 17 June to 3 July 2015. Each square is 37 cm on a side with resolution of 1 cm. Day-long samples do not start at midnight and are not shown if the images were being collected during <50% of the period.

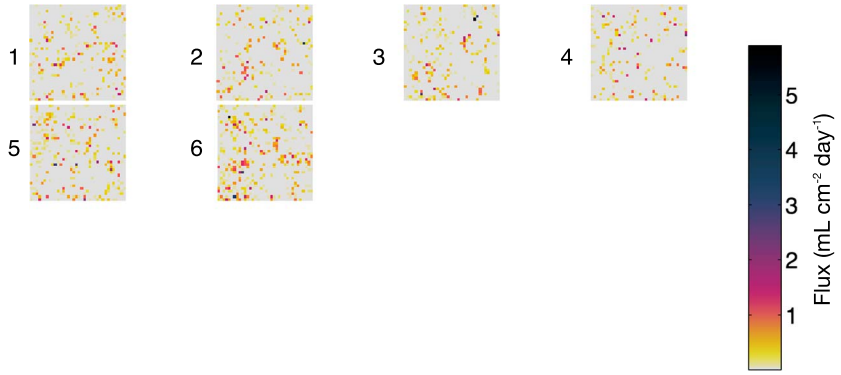

Figure 16. Calendar of daily ebullitive flux maps from Experiment 3, 10–16 July 2015. Each square is 37 cm on a side with resolution of 1 cm. Day-long samples do not start at midnight and are not shown if the images were being collected during <50% of the period.

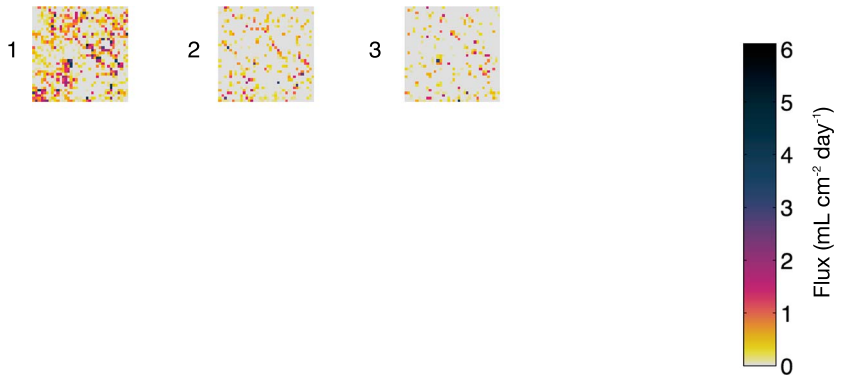

Figure 17. Calendar of daily ebullitive flux maps from Experiment 4, 10–14 September 2015. Each square is 37 cm on a side with resolution of 1 cm. Day-long samples do not start at midnight and are not shown if the images were being collected during <50% of the period.

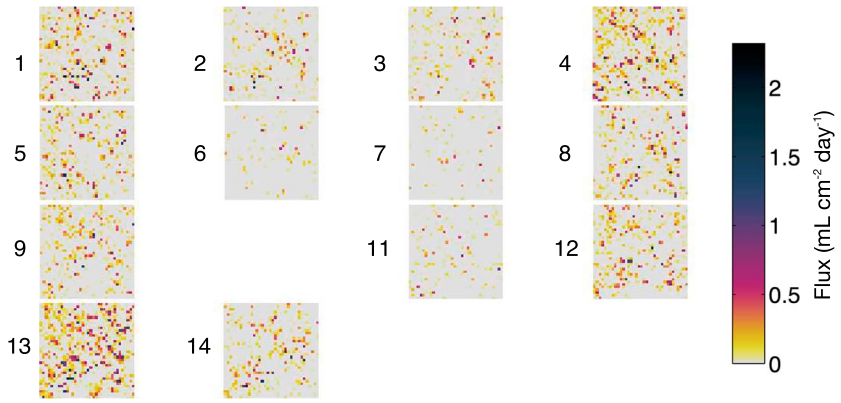

Figure 18. Calendar of daily ebullitive flux maps from Experiment 5, 12–27 February 2016. Each square is 37 cm on a side with resolution of 1 cm. Day-long samples do not start at midnight and are not shown if the images were being collected during <50% of the period.

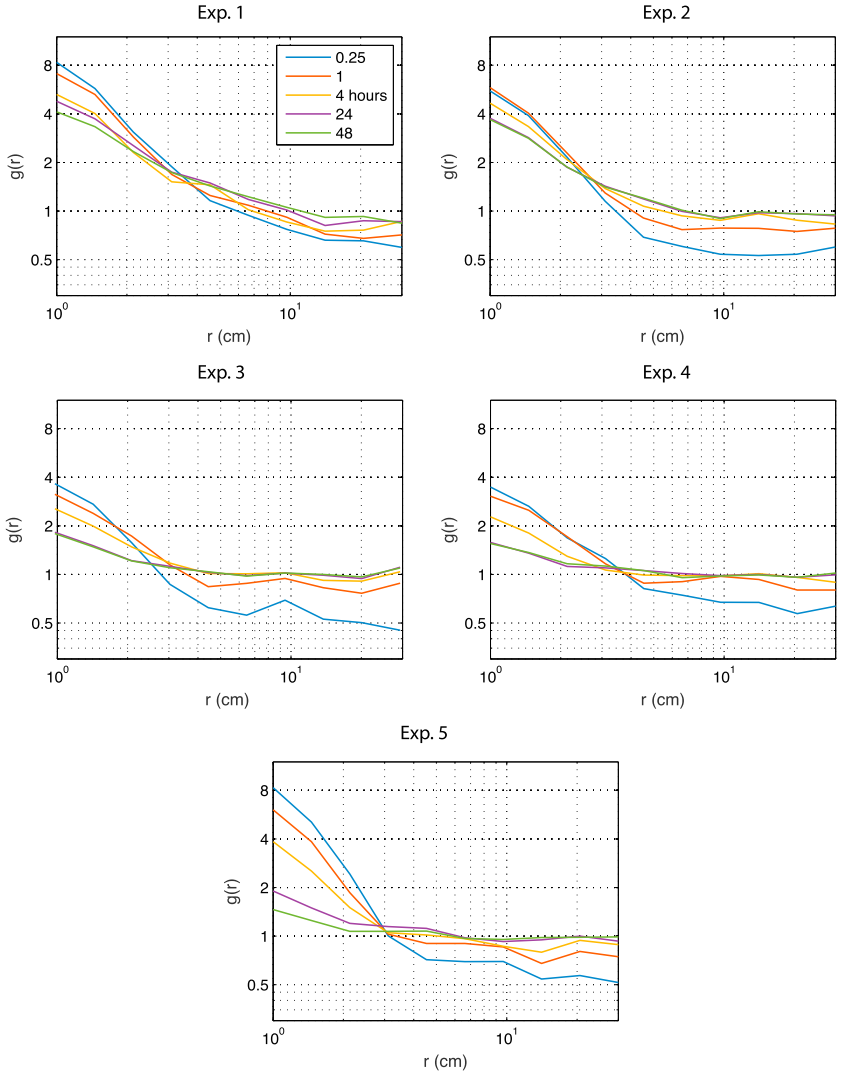

Figure 19. Radial distribution functions for Experiments 1–5 show decay of $g(r)$ with increasing r, which is characteristic of short-range clustering and long-range spacing relative of a spatially homogeneous process. Experiments 1 and 2 show clustering that is stronger and more persistent than Experiments 3–5. Experiment 5 also shows strong clustering (g(1cm)>8) over 0.25 h intervals but decays to a nearly homogeneous signal over 48 h intervals.

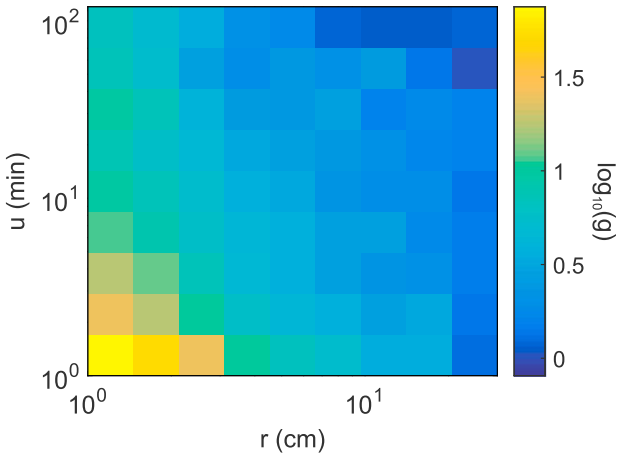

Figure 20. Spatiotemporal RDF for Experiment 1. Note the logarithmic color scale. The strong spatiotemporal clustering for $r \leq 3$ cm and $\tau \leq 2$ min suggests that ebullition episodes are often compact in space and time, although significant activity within a spatial cluster can persist even following breaks of at least 2 h. Other experiments showed qualitatively similar behavior (see SI).

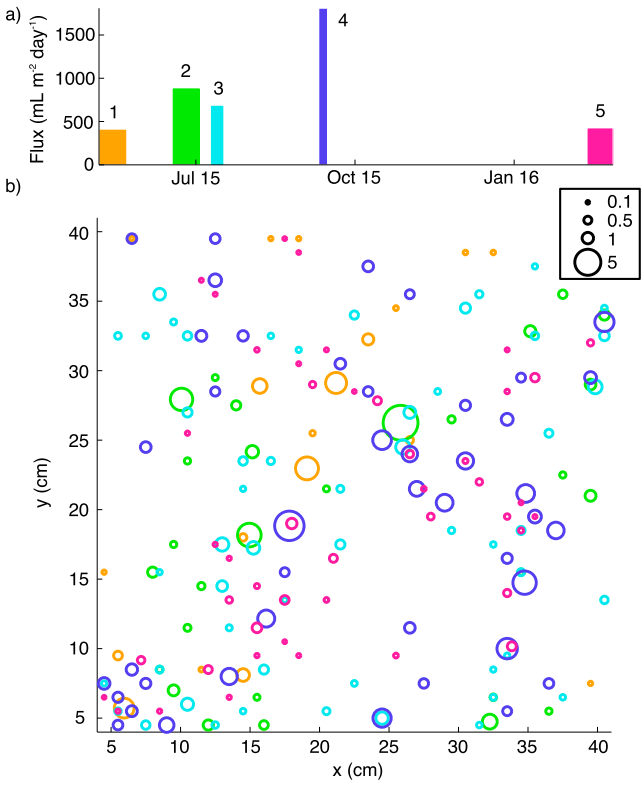

Figure 21. (a) Time series showing the timing and average flux for each of the five experiments. (b) Map showing locations of hot spot outlets from all experiments. The area of each circle is proportional to the mean flow rate through that outlet over its respective experiment (size key top right in black indicates flow rates in mL/d), and the color of each circle reflects the experiment during which it occurred, as indicated in Figure 21a subfigure.

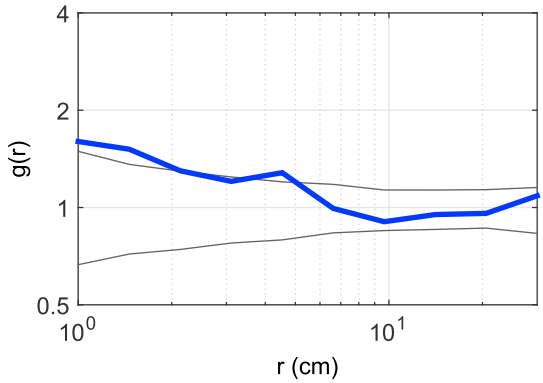

Figure 22. RDF of major outlets over all experiments (blue) shows mild short-range clustering ($g > 1$ for $r \leq 6$ cm). Some regions appear to host enhanced activity, such as ($x = 26, y = 26$) and ($x = 6, y = 6$). The spatial clustering that characterizes this activity is significant relative to 95% confidence bounds for a CSR process (gray) for $r < 2$ cm and $r \approx 4$ cm, meaning that the clustering likely arises from a non-CSR process. The CSR process was simulated with 500 Monte Carlo replicates, and the gray lines represent the 2.5th and 97.5th percentiles.

4. Discussion

4.1. Flux Magnitudes in Lab and Field Scales

The long-term spatiotemporal average flux of all experiments was approximately 0.06 mL cm^{-2} d^{-1} or 600 mL m^{-2} d^{-1}. This value is large compared with the mean ebullitive flux inferred from multimonth deployments of a lake-bottom sonar lander in 2012, 10 mL m^{-2} d^{-1} [*Scandella et al.*, 2016], as well as five-bubble traps deployed on the lake surface in 2008, 15 mL m^{-2} d^{-1} [*Scandella et al.*, 2011]. The majority of the experiments were carried out with hydrostatic triggering of ebullition following a period of high water level to inhibit ebullition and allow a buildup of stored gas in the sediments, which almost certainly increased the fluxes during the experiments relative to the long-term average. A more appropriate comparison, then, is with the average flux during high-flux events from the sonar record (defined as having a spatial mean flux above the long-term average, with 20 min binning). These high-flux events had an average of 30 mL m^{-2} d^{-1}, which is larger but still 20 times smaller than the fluxes from the incubation experiment.

The discrepancy between flux estimates may be explained with a combination of factors increasing the flux in the tank and potential underestimation of flux by the sonar. The increased rate of ebullition in the tank may be attributed to a combination of higher temperature for incubation (20–22°C in the laboratory versus 4–6° C in the hypolimnion of UML [*Varadharajan*, 2009]), increased availability of organic matter and a more uniform depth profile of methanogenesis. Both of the latter two effects may have been caused by reconstituting of the sediments. Previous studies have demonstrated the temperature dependence of methane generation and emissions [*Crill and Martens*, 1983; *Yvon-Durocher et al.*, 2014], although in some cases the resultant increase in methane oxidation can balance this effect and even reduce sediment methane concentrations [*Duc et al.*, 2010; *Fuchs et al.*, 2016]. The sonar may also underestimate fluxes due to limitations in sensitivity to small bubbles, though those did not contribute significantly to the flux in the tank (Figure 4). The sonar signal could also underestimate the flux if the method of rejecting anchor signals spuriously rejected strong bubble events, though a validation data set indicated that the sensitivity of the method (fraction of bubble volume identified as bubbles, not anchors) was above 99% (see supporting information of *Scandella et al.* [2016]).

4.2. Impacts of Incubation Conditions on Ebullition

The results presented here are applicable for other settings with fine-grained organic sediments, such are likely to be found in many other methane-generating lakes. Where the sediments are dominated by larger grain sizes, we would expect different temporal and spatial organization due to different feedbacks between solid and fluid mechanics [*Boles et al.*, 2001; *Varas et al.*, 2011; *Ramos et al.*, 2015].

The vertical distribution of bubbles trapped within the sediments may have been impacted by two competing effects of the incubation setup. The initiation of the tank with reconstituted sediments provided a source of organic carbon that was roughly uniform in the vertical, compared with the natural process of sedimentation that would deplete the deeper sediments of labile organic carbon. We expect that this effect caused bubbles to be generated faster within the deep sediments than in the lake. On the other hand, the likely saturation of

the overlying water with methane (as supported by observations of persistent bubbles trapped against the top plate) may have reduced a vertical gradient of methane observed within the pore water of natural sediments in UML, where the bottom-water methane concentration was only ≈10% of saturation [*Varadharajan*, 2009]. This second effect would have supported the formation of bubbles in shallow sediments relative to the lake. While the vertical distribution of bubbles could have impacted the spacing and persistence of conduits and outlets, measurements to reconcile the impact of these two competing effects were not available.

4.3. Hydrostatic Control

The spatially averaged time series for the five experiments show that high or rising hydrostatic pressure inhibits ebullition and low or falling pressure triggers it, when the sediments are not likely substantially depleted of gas. During cycles of pressure variation at roughly daily frequency and with magnitude <0.3 m of water column, the ebullitive flux varied continuously in a roughly anticorrelated manner with hydrostatic pressure (Figures 7 and 9). Raising the pressure by >0.3 m of water and maintaining that level was able to inhibit significant ebullition for at least 5 days (Figure 5), but it is likely that after a prolonged period at that level the gas bubbles would reach sufficient pressure and size to overcome the tensile strength of the sediment and force their way out. Conversely, lowering the pressure and keeping it low caused a large spike in the ebullition rate (Figures 5, 6, and 8).

Despite the clear impact of hydrostatic pressure on gas flux, the linear relationship was weak in all experiments ($R^2 < 0.35$, Table 1), and we infer that the role of hydrostatic pressure is mediated by the presence of gas within the sediments. During Experiment 1, an extended period of intense ebullition (≥0.2 mL cm^{-2} d^{-1} for >1 day) was followed by a continuous period of quiescence (≤0.02 mL cm^{-2} d^{-1} for >6 days). This quiescence persisted even during a >20 cm drop in hydrostatic pressure, which was large enough to trigger ebullition events in Experiments 2, 3, and 5 (and perhaps in Experiment 1). The inability to trigger ebullition even with a significant hydrostatic pressure drop suggests a second control on ebullition, and the seemingly most likely control given the preceding high-flux episode is that the sediments had been depleted of gas.

The demonstration of hydrostatic control of ebullition is consistent with previous observations at the field scale [*Strayer and Tiedje*, 1978; *Martens and val Klump*, 1980; *Kipphut and Martens*, 1982; *Chanton et al.*, 1989; *Fechner-Levy and Hemond*, 1996; *Tokida et al.*, 2007; *Torres et al.*, 2002; *Yamamoto et al.*, 2009; *Varadharajan and Hemond*, 2012], as well as with a mechanistic model explaining how the hydrostatic forcing is mediated by the effective stress [*Scandella et al.*, 2011]. A recent demonstration of hydrostatic control of ebullition from estuarine wetland sediments in laboratory conditions appears at first to contrast with our results by showing stronger triggering of ebullition during rising tides than during falling tides [*Chen and Slater*, 2016]. However, these apparently contradictory results were also explained by effective stress control of ebullition, because the effective stress may become more compressive when the water level falls *below* the sediment surface and then becomes more tensile when the water level begins to rise again [*Chen and Slater*, 2016].

4.4. Temporal Clustering

Ebullition events and bubble arrivals are clustered in time relative to a Poisson process over a range of spatial scales (3 cm–8 m), consistent with a process of reduction and healing of sediment tensile strength following bubble passage. The distribution of interarrival times, as quantified using the hazard function, shows power law decay for pixels of size 3 and 37 cm. This power law decay can be modeled as a Weibull process, used in failure analysis to model a collection of components that show premature failure (in this case bubble emission) and increasing reliability (here absence of bubble release) with time. We propose that the gradual increase in reliability is consistent with healing of sediment tensile strength following bubble passage, making it progressively less likely that a bubble will have sufficient pressure to reduce the effective stress and force the grains apart with time. This means that conduits are less likely to be reused as they spend a longer time inactive.

One difference between our observations of short-τ temporal clustering and previous work showing recovery of yield stress [*Merckelbach et al.*, 2002] is the timescale over which these processes operate. *Merckelbach et al.* [2002] showed recovery of up to 200 Pa in yield stress over ~100 days in sediments from the Ems-Dollard estuary in The Netherlands, with a roughly linear increase over time. If tensile strength recovery is the cause of the short-term temporal clustering in our system, then its magnitude would have to be significant, even over the scale of seconds and minutes, to show an appreciable decline in $h(\tau)$ over those timescales. The power law scaling of $h(\tau)$ suggests that σ_T could recover as $\tau^{1-\beta}$ so that the initial rate of recovery could be larger than the late-term recovery scale, but if the work above is used to estimate the magnitude of the late-term recovery (200 Pa in 100 days), then for $\beta \approx 0.4$, the amount of recovery at 1 h would only be 4 Pa. Such stress is small

relative even to the buoyancy of a 1 cm bubble, ~100 Pa. Therefore, tensile strength recovery alone does not appear to be a sufficient explanation for the temporal clustering. Other mechanisms that could mediate bubble release over short timescales include viscous behavior of the sediment-water matrix [*Boudreau et al.*, 2005; *Algar et al.*, 2011a, 2011b] and disturbance of nearby surrounding sediments with bubble motion, triggering or facilitating aftershock mobilization.

4.5. Spatial Clustering

The spatial signature of ebullition from sediments at the submeter scale is characterized by outlets that are most active over bursts of 1–2 min (Figure 20) but are capable of persisting for days (Figure 19) and even months (Figure 22). This persistence is surprising because spatial clusters at the field scale (radius 1–3 m) only dominated the spatial distribution of gas flux over hours or days, even in undisturbed sediments observed in situ [*Scandella et al.*, 2011]. The timescale of persistence is long relative to the timescale for regenerating a store of trapped bubbles after exhausting it, as we infer occurred between Experiments 1 and 2 (Figures 5 and 21). The sediments used in this experiment were reconstituted, and while it is strictly possible that the methanogenesis rate was influenced by the spatial distribution of microbial consortia [*Hoehler et al.*, 1994], we expect that these would have been plentiful enough to be homogeneously distributed. Also, while we cannot completely rule out the possibility of bioturbation, the experimental conditions likely prevented the survival of infauna.

We can rationalize the persistence of fine-scale heterogeneity as the product of a process where gas is transported laterally toward outlets from the surrounding sediments. Even if conduits are initially reused due to sediment mechanics, their persistence over the timescale of bubble generation (apparently weeks to months) requires a mechanism by which they could be supplied with methane. If the conduit spacing is limited by diffusive mass flux toward each conduit, the length scale is expected to be on the order of ≈5–7 cm for diffusion over ~1 month between major ebullition events, and this distance is similar to the spacing of the major outlets in later experiments (Table 2). The earlier experiments (1 and 2) showed slightly fewer, more distant outlets, and the progression toward more densely spaced outlets over the 10 months that were spanned by the five experiments may be indicative of development of a more ramified conduit network that allows gas to escape from a greater number of (more densely spaced) locations.

5. Conclusions

Our novel laboratory incubation has demonstrated the persistence of bubble outlets over multiple cycles of both hydrostatically driven ebullition and bubble formation and depletion within soft, methane-generating sediments. This persistence of outlets is significant because it arose in reconstituted sediments and therefore is unlikely to derive from heterogeneity in the sediment mechanical properties or methane generation rate. Instead, we propose that conduits are supplied via diffusion from the surrounding sediments, and the spacing of outlets is controlled by the length scale of diffusive transport between major ebullition events. The conceptual model of outlets whose spacing is controlled by "competition" for methane evokes other spatial patterns, such as discrete vegetation patches competing for water in arid environments [*Getzin et al.*, 2016]. Meanwhile, future research should investigate the degree to which these transport processes control the distribution of ebullition in more natural systems, with a more heterogeneous methane source and distribution of sediment mechanical properties, as well as additional processes such as bioturbation at play.

The observation of temporally clustered ebullition with power law decay in the hazard function is qualitatively consistent with the hypothesized mechanism of slow healing of sediment tensile strength following its drop with bubble passage. However, the rapid drop in hazard over the scale of hours is faster than expected given previous measurements of slowly rebounding sediment yield stress [*Merckelbach et al.*, 2002]. This mismatch suggests that other mechanisms may also play a role, such as localized sediment disturbance and viscous sediment deformation, and investigating these may prove a fruitful avenue for further study.

The fine-scale spatial and temporal concentration of bubble releases implies that the atmospheric methane flux is indeed moderated by the physics of gas bubble generation and mobilization within the sediments. This work motivates further study into the impact of multiple bubble releases on bubble rise and methane dissolution into the water column, and a better-refined picture of methane delivery is expected to improve our understanding of the biogeochemical cycles at play in these dynamic environments [*Preheim et al.*, 2016] and the role that lakes play in the greenhouse effect.

Acknowledgments
We thank Charles Harvey and John MacFarlane at MIT, and John Pohlman and Carolyn Ruppel at the USGS for insightful discussions. This work was supported by the U.S. National Science Foundation (award 1045193) and the U.S. Department of Energy (grant DE-FE0013999). The data associated with this study can be accessed at a dedicated webpage (http://juanesgroup.mit.edu/publications/methaneincubation), where links to the data sets are provided, and a description of those data sets is given.

References

Algar, C. K., B. P. Boudreau, and M. A. Barry (2011a), Initial rise of bubbles in cohesive sediments by a process of viscoelastic fracture, *J. Geophys. Res.*, *116*, B04207, doi:10.1029/2010JB008133.
Algar, C. K., B. P. Boudreau, and M. A. Barry (2011b), Release of multiple bubbles from cohesive sediments, *Geophys. Res. Lett.*, *38*, L08606, doi:10.1029/2011GL046870.
Bastviken, D., J. Cole, M. Pace, and L. Tranvik (2004), Methane emissions from lakes: Dependence of lake characteristics, two regional assessments, and a global estimate, *Global Biogeochem. Cycles*, *18*, GB4009, doi:10.1029/2004GB002238.
Bastviken, D., L. J. Tranvik, J. A. Downing, P. M. Crill, and A. Enrich-Prast (2011), Freshwater methane emissions offset the continental carbon sink, *Science*, *331*(6013), 50.
Bayrakci, G., et al. (2014), Acoustic monitoring of gas emissions from the seafloor. Part II: A case study from the Sea of Marmara, *Mar. Geophys. Res.*, *35*(3), 211–229.
Boles, J., J. Clark, I. Leifer, and L. Washburn (2001), Temporal variation in natural methane seep rate due to tides, Coal Oil Point area, California, *J. Geophys. Res.*, *106*(C11), 27,077–27,086.
Boudreau, B., C. Algar, B. Johnson, I. Croudace, A. Reed, Y. Furukawa, K. Dorgan, P. Jumars, A. Grader, and B. Gardiner (2005), Bubble growth and rise in soft sediments, *Geology*, *33*(6), 517–520.
Chanton, J., C. Martens, and C. Kelley (1989), Gas transport from methane-saturated, tidal freshwater and wetland sediments, *Limnol. Oceanogr.*, *34*(5), 807–819.
Chen, X., and L. Slater (2016), Methane emission through ebullition from an estuarine mudflat: 1. A conceptual model to explain tidal forcing based on effective stress changes, *Water Resour. Res.*, *52*, 4469–4485, doi:10.1002/2015WR018058.
Comas, X., and W. Wright (2012), Heterogeneity of biogenic gas ebullition in subtropical peat soils is revealed using time-lapse cameras, *Water Resour. Res.*, *48*, W04601, doi:10.1029/2011WR011654.
Crill, P., and C. Martens (1983), Spatial and temporal fluctuations of methane production in anoxic coastal marine sediments, *Limnol. Oceanogr.*, *28*(6), 1117–1130.
Crill, P., K. Bartlett, J. Wilson, D. Sebacher, R. Harriss, J. Melack, S. Macintyre, L. Lesack, and L. Smithmorrill (1988), Tropospheric methane from an Amazonian floodplane lake, *J. Geophys. Res.*, *93*(D2), 1564–1570.
Daszykowski, M., B. Walczak, and D. Massart (2001), Looking for natural patterns in data—Part 1. Density-based approach, *Chemom. Intell. Lab. Syst.*, *56*(2), 83–92.
DelSontro, T., D. F. McGinnis, S. Sobek, I. Ostrovsky, and B. Wehrli (2010), Extreme methane emissions from a Swiss hydropower reservoir: Contribution from bubbling sediments, *Environ. Sci. Technol.*, *44*(7), 2419–2425.
DelSontro, T., D. F. McGinnis, B. Wehrli, and I. Ostrovsky (2015), Size does matter: Importance of large bubbles and small-scale hot spots for methane transport, *Environ. Sci. Technol.*, *49*(3), 1268–1276.
Delwiche, K., S. Senft-Grupp, and H. Hemond (2015), A novel optical sensor designed to measure methane bubble sizes in situ, *Limnol. Oceanogr. Methods*, *13*(12), 712–721.
Dieterich, J. H. (1979), Modeling of rock friction: 1. Experimental results and constitutive equations, *J. Geophys. Res.*, *84*(B5), 2161–2168.
Duc, N. T., P. Crill, and D. Bastviken (2010), Implications of temperature and sediment characteristics on methane formation and oxidation in lake sediments, *Biogeochemistry*, *100*(1–3), 185–196.
Fechner-Levy, E., and H. Hemond (1996), Trapped methane volume and potential effects on methane ebullition in a northern peatland, *Limnol. Oceanogr.*, *41*(7), 1375–1383.
Forster, P., et al. (2007), Changes in atmospheric constituents and in radiative forcing, in *Climate Change 2007: The Physical Science Basis. Contribution of Working Group I to the Fourth Assessment Report of the Intergovernmental Panel on Climate Change*, edited by S. Solomon et al., pp. 129–234, Cambridge Univ. Press, Cambridge, U. K., and New York.
Fuchs, A., E. Lyautey, B. Montuelle, and P. Casper (2016), Effects of increasing temperatures on methane concentrations and methanogenesis during experimental incubation of sediments from oligotrophic and mesotrophic lakes, *J. Geophys. Res. Biogeosci.*, *121*, 1394–1406, doi:10.1002/2016JG003328.
Gardiner, B., B. Boudreau, and B. Johnson (2003), Growth of disk-shaped bubbles in sediments, *Geochim. Cosmochim. Acta*, *67*(8), 1485–1494.
Getzin, S., et al. (2016), Discovery of fairy circles in Australia supports self-organization theory, *Proc. Natl. Acad. Sci. U.S.A.*, *113*(13), 3551–3556.
Gong, X., S. Takagi, and Y. Matsumoto (2009), The effect of bubble-induced liquid flow on mass transfer in bubble plumes, *Int. J. Multiphase Flow*, *35*(2), 155–162.
Greinert, J. (2008), Monitoring temporal variability of bubble release at seeps: The hydroacoustic swath system GasQuant, *J. Geophys. Res.*, *113*, C07048, doi:10.1029/2007JC004704.
Greinert, J., and B. Nutzel (2004), Hydroacoustic experiments to establish a method for the determination of methane bubble fluxes at cold seeps, *Geo-Mar. Lett.*, *24*(2), 75–85.
Greinert, J., D. F. McGinnis, L. Naudts, P. Linke, and M. De Batist (2010), Atmospheric methane flux from bubbling seeps: Spatially extrapolated quantification from a Black Sea shelf area, *J. Geophys. Res.*, *115*, C01002, doi:10.1029/2009JC005381.
Hoehler, T., M. Alperin, D. Albert, and C. Martens (1994), Field and laboratory studies of methane oxidation in an anoxic marine sediment—Evidence for a methanogen-sulfate reducer consortium, *Global Biogeochem. Cycles*, *8*(4), 451–463.
Holtz, R. D., and W. D. Kovacs (2010), *An Introduction to Geotechnical Engineering*, Prentice Hall, West Sussex, N. J.
Illian, J., A. Penttinen, H. Stoyan, and D. Stoyan (2008), *Statistical Analysis and Modelling of Spatial Point Patterns*, Wiley, West Sussex, U. K.
Jain, A. K., and R. Juanes (2009), Preferential mode of gas invasion in sediments: Grain-scale mechanistic model of coupled multiphase fluid flow and sediment mechanics, *J. Geophys. Res.*, *114*, B08101, doi:10.1029/2008JB006002.
Keller, M., and R. Stallard (1994), Methane emission by bubbling from Gatun Lake, Panama, *J. Geophys. Res.*, *99*(D4), 8307–8319.
Kipphut, G., and C. Martens (1982), Biogeochemical cycling in an organic-rich coastal marine basin. 3. Dissolved gas transport in methane-saturated sediments, *Geochim. Cosmochim. Acta*, *46*(11), 2049–2060.
Kirschke, S., et al. (2013), Three decades of global methane sources and sinks, *Nat. Geosci.*, *6*(10), 813–823.
Klein, S. (2006), Sediment porewater exchange and solute release during ebullition, *Mar. Chem.*, *102*(1–2), 60–71.
Kong, X.-Z., W. Kinzelbach, and F. Stauffer (2009), Migration of air channels: An instability of air flow in mobile saturated porous media, *Chem. Eng. Sci.*, *64*(7), 1528–1535.
Kong, X.-Z., W. Kinzelbach, and F. Stauffer (2010), Compaction and size segregation in a liquid-saturated grain packing due to pulsation effect during air injection, *Chem. Eng. Sci.*, *65*(9), 2680–2688.
Leifer, I., B. P. Luyendyk, J. Boles, and J. F. Clark (2006), Natural marine seepage blowout: Contribution to atmospheric methane, *Global Biogeochem. Cycles*, *20*(3), GB3008, doi:10.1029/2005GB002668.

Leitch, A., and W. Baines (1989), Liquid volume flux in a weak bubble plume, *J. Fluid Mech.*, *205*, 77–98.
Lubarda, V. A., and K. A. Talke (2011), Analysis of the equilibrium droplet shape based on an ellipsoidal droplet models, *Langmuir*, *27*(17), 10,705–10,713.
Maeck, A., T. DelSontro, D. F. McGinnis, H. Fischer, S. Flury, M. Schmidt, P. Fietzek, and A. Lorke (2013a), Sediment trapping by dams creates methane emission hot spots, *Environ. Sci. Technol.*, *47*(15), 8130–8137.
Maeck, A., H. Hofmann, and A. Lorke (2013b), Pumping methane out of aquatic sediments; forcing mechanisms that affect the temporal dynamics of ebullition, *Biogeosci. Discuss.*, *10*(11), 18,687–18,722.
Martens, C., and J. val Klump (1980), Biogeochemical cycling in an organic-rich coastal marine basin. 1. Methane sediment-water exchange processes, *Geochim. Cosmochim. Acta*, *44*(3), 471–490.
Mattson, M. D., and G. Likens (1990), Air pressure and methane fluxes, *Nature*, *347*(6295), 718–719.
McGinnis, D. F., J. Greinert, Y. Artemov, S. E. Beaubien, and A. Wuest (2006), Fate of rising methane bubbles in stratified waters: How much methane reaches the atmosphere?, *J. Geophys. Res.*, *111*, C09007, doi:10.1029/2005JC003183.
Meier, J. A., J. S. Jewell, C. E. Brennen, and J. Imberger (2011), Bubbles emerging from a submerged granular bed, *J. Fluid Mech.*, *666*, 189–203.
Merckelbach, L. M. (2000), Consolidation and strength evolution of soft mud layers, PhD thesis, TU Delft, Netherlands.
Merckelbach, L. M., C. Kranenburg, and J. C. Winterwerp (2002), Strength modelling of consolidating mud beds, *Proc. Mar. Sci.*, *5*, 359–373.
Nakamura, T., Y. Nojiri, M. Utsumi, T. Nozawa, and A. Otsuki (1999), Methane emission to the atmosphere and cycling in a shallow eutrophic lake, *Arch. Hydrobiol.*, *144*(4), 383–407.
Ohser, J., and F. Mücklich (2000), *Statistical Analysis of Microstructures in Materials Science*, Wiley, Chichester, U. K.
Osti, G., F. Wolf, and P. Philippi (2009), Spreading of liquid drops on acrylic surfaces, in *Proceedings of the 20th International Congress of Mechanical Engineering*, International Congress of Mechanical Engineering, Gramado, RS, Brazil.
Ostrovsky, I., D. F. McGinnis, L. Lapidus, and W. Eckert (2008), Quantifying gas ebullition with echosounder: The role of methane transport by bubbles in a medium-sized lake, *Limnol. Oceanogr. Methods*, *6*, 105–118.
Preheim, S. P., S. W. Olesen, S. J. Spencer, A. Materna, C. Varadharajan, M. Blackburn, J. Friedman, J. Rodríguez, H. Hemond, and E. J. Alm (2016), Surveys, simulation and single-cell assays relate function and phylogeny in a lake ecosystem, *Nat. Microbiol.*, *1*, 16130.
Queré, D. (2005), Non-sticking drops, *Rep. Prog. Phys.*, *68*, 2495–2532.
Ramos, G., G. Varas, J.-C. Géminard, and V. Vidal (2015), Gas-induced fluidization of mobile liquid-saturated grains, *Phys. Rev. E*, *92*, 062210.
Rehder, G., P. Brewer, E. Peltzer, and G. Friederich (2002), Enhanced lifetime of methane bubble streams within the deep ocean, *Geophys. Res. Lett.*, *29*(15), 1731, doi:10.1029/2001GL013966.
Rudd, J., R. Hamilton, and N. Campbell (1974), Measurement of microbial oxidation of methane in lake waters, *Limnol. Oceanogr.*, *19*(3), 519–524.
Ruina, A. (1983), Slip instability and state variable friction laws, *J. Geophys. Res.*, *88*(B12), 10,359–10,370.
Scandella, B. P., C. Varadharajan, H. F. Hemond, C. Ruppel, and R. Juanes (2011), A conduit dilation model of methane venting from lake sediments, *Geophys. Res. Lett.*, *38*, L06408, doi:10.1029/2011GL046768.
Scandella, B. P., L. Pillsbury, T. Weber, C. Ruppel, H. F. Hemond, and R. Juanes (2016), Ephemerality of discrete methane vents in lake sediments, *Geophys. Res. Lett.*, *43*, 4374–4381, doi:10.1002/2016GL068668.
Schmidt, K. A. G., G. K. Folas, and B. Kvamme (2007), Calculation of the interfacial tension of the methane-water system with the linear gradient theory, *Fluid Phase Equilib.*, *261*(1–2), 230–237.
Schneider von Deimling, J., J. Greinert, N. R. Chapman, W. Rabbel, and P. Linke (2010), Acoustic imaging of natural gas seepage in the North Sea: Sensing bubbles controlled by variable currents, *Limnol. Oceanogr. Methods*, *8*, 155–171.
Skarke, A. D., C. D. Ruppel, M. Kodis, D. Brothers, and E. Lobecker (2014), Widespread methane leakage from the sea floor on the northern US Atlantic margin, *Nat. Geosci.*, *7*(9), 657–661.
Spliethoff, H., and H. Hemond (1996), History of toxic metal discharge to surface waters of the Aberjona Watershed, *Environ. Sci. Technol.*, *30*(1), 121–128.
Stapelberg, R. F. (2009), *Handbook of Reliability, Availability, Maintainability and Safety in Engineering Design*, Springer, London.
Strayer, R., and J. Tiedje (1978), In situ methane production in a small, hypereutrophic, hard-water lake: Loss of methane from sediments by vertical diffusion and ebullition, *Limnol. Oceanogr.*, *23*(6), 1201–1206.
Tokida, T., T. Miyazaki, M. Mizoguchi, O. Nagata, F. Takakai, A. Kagemoto, and R. Hatano (2007), Falling atmospheric pressure as a trigger for methane ebullition from peatland, *Global Biogeochem. Cycles*, *21*, GB2003, doi:10.1029/2006GB002790.
Torres, M., J. McManus, D. Hammond, M. de Angelis, K. Heeschen, S. Colbert, M. Tryon, K. Brown, and K. Suess (2002), Fluid and chemical fluxes in and out of sediments hosting methane hydrate deposits on Hydrate Ridge, OR. I: Hydrological provinces, *Earth Planet. Sci. Lett.*, *201*(3–4), 525–540.
Vallebuona, G., A. Casali, and W. Kracht (2005), Characterization and modeling of bubbles size distribution in mechanical flotation cells, *Rev. Metal.*, *41*(4), 243–250.
Varadharajan, C. (2009), Magnitude and spatio-temporal variability of methane emissions from a eutrophic freshwater lake, PhD thesis, Massachusetts Institute of Technology, Cambridge, Mass.
Varadharajan, C., and H. F. Hemond (2012), Time-series analysis of high-resolution ebullition fluxes from a stratified, freshwater lake, *J. Geophys. Res.*, *117*, G02004, doi:10.1029/2011JG001866.
Varas, G., V. Vidal, and J.-C. Geminard (2009), Dynamics of crater formations in immersed granular materials, *Phys. Rev. E*, *79*(2), 021301.
Varas, G., V. Vidal, and J.-C. Géminard (2011), Venting dynamics of an immersed granular layer, *Phys. Rev. E*, *83*(1), 011302.
Walter, K. M., S. A. Zimov, J. P. Chanton, D. Verbyla, and F. S. Chapin III (2006), Methane bubbling from Siberian thaw lakes as a positive feedback to climate warming, *Nature*, *443*, 71–75.
Walter Anthony, K. M., and P. Anthony (2013), Constraining spatial variability of methane ebullition seeps in thermokarst lakes using point process models, *J. Geophys. Res. Biogeosci.*, *118*, 1015–1034, doi:10.1002/jgrg.20087.
Wang, B., S. A. Socolofsky, J. A. Breier, and J. S. Seewald (2016), Observations of bubbles in natural seep flares at MC 118 and GC 600 using in situ quantitative imaging, *J. Geophys. Res. Oceans*, *121*, 2203–2230, doi:10.1002/2015JC011452.
Wiegand, T., and K. A. Moloney (2014), *Handbook of Spatial Point Pattern Analysis*, Chapman and Hall, Boca Raton, Fla.
Wik, M., P. M. Crill, D. Bastviken, A. Danielsson, and E. Norback (2011), Bubbles trapped in arctic lake ice: Potential implications for methane emissions, *J. Geophys. Res. Biogeosci.*, *116*, G03044, doi:10.1029/2011JG001761.

Yamamoto, A., M. Hirota, S. Suzuki, Y. Oe, P. Zhang, and S. Mariko (2009), Effects of tidal fluctuations on CO_2 and CH_4 fluxes in the littoral zone of a brackish-water lake, *Limnology*, *10*(3), 228–237.

Yuan, Q., K. T. Valsaraj, D. D. Reible, and C. S. Willson (2007), A laboratory study of sediment and contaminant release during gas ebullition, *J. Air Waste Manage. Assoc.*, *57*(9), 1103–1111.

Yvon-Durocher, G., A. P. Allen, D. Bastviken, R. Conrad, C. Gudasz, A. St-Pierre, N. Thanh-Duc, and P. A. del Giorgio (2014), Methane fluxes show consistent temperature dependence across microbial to ecosystem scales, *Nature*, *507*, 488–491.

Supporting Information for

"Persistence of bubble outlets in soft, methane-generating sediments"

Benjamin P. Scandella[1], **Kyle Delwiche**[1], **Harold Hemond**[1], **Ruben Juanes**[1,2]

[1]Department of Civil and Environmental Engineering, Massachusetts Institute of Technology, Cambridge, Massachusetts, USA.

[2]Department of Earth, Atmospheric and Planetary Sciences, Massachusetts Institute of Technology, Cambridge, Massachusetts, USA.

Contents

1. Gas chromatograph calibration (Fig. S1)
2. Spatial precision
3. Spatiotemporal radial distribution functions (ST-RDF) for Experiments 2–5 (Fig. S2)

Gas chromatograph calibration

The gas released from the tank was analyzed for CH_4, CO_2 and N_2 content using a gas chromatograph thermal conductivity detector (TCD). The unit was calibrated using methane standards of 0%, 10%, 50% and 100%, and the standards fit calibrations lines with $R^2 \geq 0.9968$ (Fig. S1). Nitrogen calibrations were carried out using standards of 0%, 10%, and 50%, with air as a treated as a standard with concentration 78%. Although the TCD was not specifically calibrated for oxygen, concentrations were quite low and likely reflect gas that entered the bubbles via minor leakage in the collection tube or during gas sampling and storage.

Spatial precision

The accuracy of the location estimates is impacted by both the effectiveness of the image segmentation and the rate at which images were acquired. Bubbles rise vertically through the open water and then quickly transition to lateral (typically upslope) motion, so the location of a bubble in the first image where it is detected may be displaced in the upslope direction from the outlet location. Large bubbles also often appeared just before touching the tank top, as a faint bright spot in images (for example, this occurred for 66% of the largest 58 bub-

Corresponding author: Ruben Juanes, juanes@mit.edu

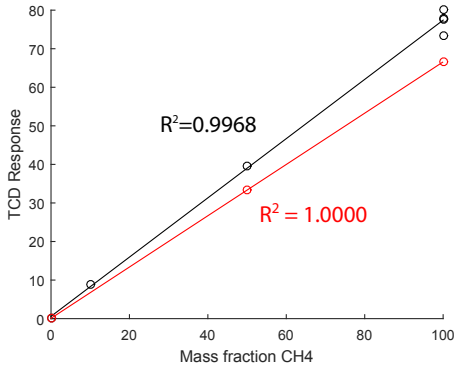

Figure S1. Calibration data for gas chromatograph thermal conductivity detector (TCD) used to analyze methane content of gas collected from the incubation tank. Two separated calibration runs were used to account for instrument drift over the ≈2 hour analysis period. 0% methane standards were used for both calibrations.

bles in Experiment 1). The locations of these below-tank-top bright spots are unaffected by the upslope migration so better represent the bubble outlet location than bubbles that had already hit the top and potentially proceeded upslope some distance before being imaged. The below-tank-top locations still do not perfectly represent bubble outlets because bubbles larger than 4 mm in diameter rise in a wobble pattern with displacement on the order of 1 cm [*Zeng and Cai*, 2014], but the error introduced by the wobble is isotropic. As a result, the locations of faint below-tank-top locations were compared against the locations of the first arrival against the tank top plate, for the largest 58 bubbles detected during Experiment 1, in order to estimate the magnitude of the error up-slope migration. The magnitude was found to be 2 ± 1 cm (mean±1 standard deviation, max 5.6 cm), and this represents an upper bound on the error because the sub-tank-top images were automatically identified as the original bubble location for 40% of these largest bubbles. This magnitude is comparable to the 1-cm resolution of the method and small enough that distinct hot-spots are still discernible.

Spatiotemporal radial distribution functions for all experiments: Fig. S2

References

Zeng, Q., and J. Cai (2014), Three-dimension simulation of bubble behavior under nonlinear oscillation, *Annals of Nuclear Energy*, *63*, 680–690.

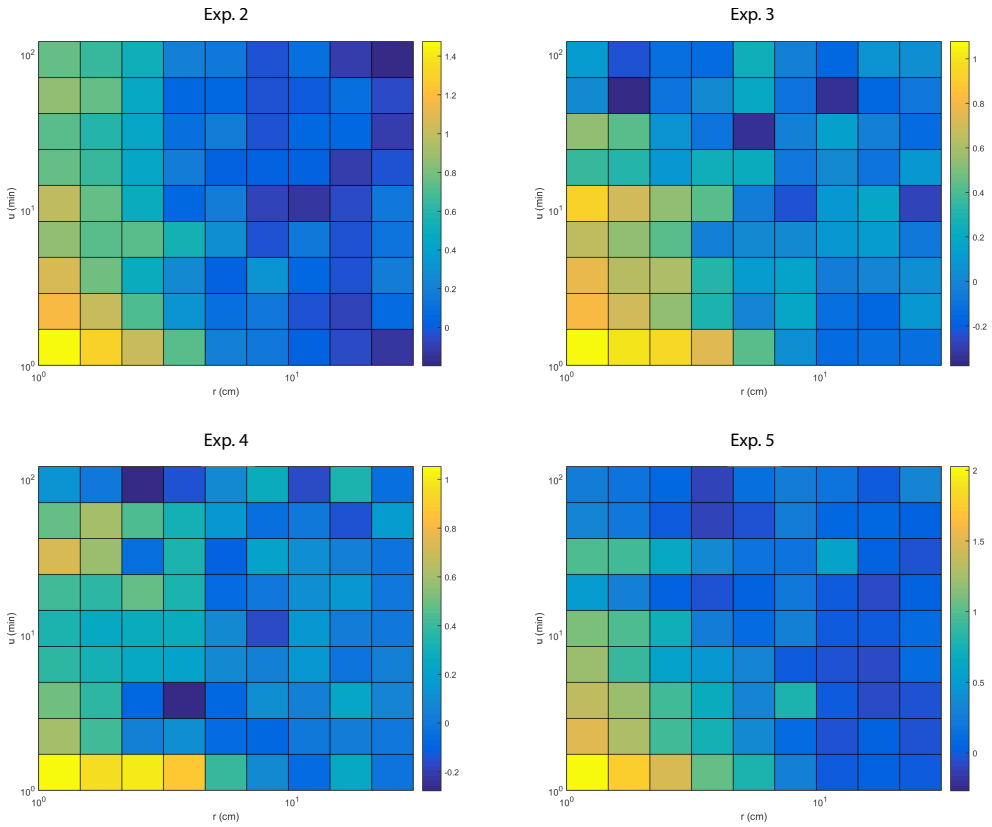

Figure S2. Spatiotemporal radial distribution functions from Experiments 2–5, show qualitatively similar patterns to that from Experiment 1 (Fig. 20 from the main text). Note the different scales on the color bars, which all measure $\log_1 0(g)$ but to different limits.